



Article scientifique

Article

2021

Published version

Open Access

This is the published version of the publication, made available in accordance with the publisher's policy.

Enhanced single-node lattice Boltzmann boundary condition for fluid flows

Marson, Francesco; Thorimbert, Yann; Chopard, Bastien; Ginzburg, Irina; Latt, Jonas

How to cite





MARSON, Francesco et al. Enhanced single-node lattice Boltzmann boundary condition for fluid flows.
In: Physical Review. E, 2021, vol. 103, n° 053308. doi: 10.1103/PhysRevE.103.053308

This publication URL: <https://archive-ouverte.unige.ch//unige:151868>

Publication DOI: [10.1103/PhysRevE.103.053308](https://doi.org/10.1103/PhysRevE.103.053308)

© The author(s). This work is licensed under a Other Open Access license

<https://www.unige.ch/biblio/aou/fr/guide/info/references/licences/>

Enhanced single-node lattice Boltzmann boundary condition for fluid flowsFrancesco Marson ^{1,*}, Yann Thorimbert,¹ Bastien Chopard,¹ Irina Ginzburg ² and Jonas Latt ¹¹*Department of Computer Science, University of Geneva, 1204 Geneva, Switzerland*²*Paris-Saclay University, INRAE, UR HYCAR, 92160, Antony, France* (Received 25 September 2020; revised 31 January 2021; accepted 29 March 2021; published 21 May 2021)

We propose a procedure to implement Dirichlet velocity boundary conditions for complex shapes that use data from a single node only, in the context of the lattice Boltzmann method. Two ideas are at the base of this approach. The first is to generalize the geometrical description of boundary conditions combining bounce-back rule with interpolations. The second is to enhance them by limiting the interpolation extension to the proximity of the boundary. Despite its local nature, the resulting method exhibits second-order convergence for the velocity field and shows similar or better accuracy than the well-established Bouzidi's scheme for curved walls [M. Bouzidi, M. Firdaouss, and P. Lallemand, *Phys. Fluids* **13**, 3452 (2001)]. Among the infinite number of possibilities, we identify several meaningful variants of the method, discerned by their approximation of the second-order nonequilibrium terms and their interpolation coefficients. For each one, we provide two parametrized versions that produce viscosity independent accuracy at steady state. The method proves to be suitable to simulate moving rigid objects or surfaces moving following either the rigid body dynamics or a prescribed kinematic. Also, it applies uniformly and without modifications in the whole domain for any shape, including corners, narrow gaps, or any other singular geometry.

DOI: [10.1103/PhysRevE.103.053308](https://doi.org/10.1103/PhysRevE.103.053308)**I. INTRODUCTION**

In recent years, the rising interest in complex flows in numerous applications such as particulate suspensions [1], porous media [2,3], blood flow [4], and multiphase flow [5] gave a new impulse to research on local boundary conditions for the lattice Boltzmann Method (LBM). Local boundary methods for curved geometries can deliver a precise flow description, needing to access the flow variables only on a *single node* located next to the surface. Thanks to these characteristics, it is possible to improve the geometry description, yet maintain an efficient memory access pattern and limit the communications between threads in parallel simulations.

Since the standard lattice Boltzmann method is inherently bounded to its regular and structured lattice, boundary conditions that aim to recover realistic shapes are often of *off-lattice* nature. This means that some information located outside the concerned mesh node demands to be integrated into the mathematical model, generally using interpolations. In the opposite case, the accuracy degenerates to first-order in space, due to the inability of the scheme to follow the curved geometry. A first-order representation deteriorates the overall accuracy of the simulation and may require an increase of mesh resolution. For example, the common *half-way bounce-back* rule [6,7] can be made third-order accurate in grid-aligned Poiseuille profile [7–9], but the solution degenerates to a first-order “stair-cased” representation when applied to curved boundaries [10,11]. The mismatch between the bulk and boundary solution excites spurious accommodation layers [12] that

population interpolations can reduce [13]. However, the use of interpolations or extrapolations causes, in most cases, the loss of locality of the method. Roughly speaking, if we call *boundary nodes* the nodes located next to the surface, then the boundary condition will need to access the second layer of nodes. Nevertheless, in the past three decades, some local curved boundary conditions have been proposed [10,14–19].

To cope with the large number of different approaches, it is useful to split boundary techniques into two groups. The first computes the unknown populations through a unique operation applied to the current node, giving rise to the *node-based* methods. The second sequentially resolves the unknowns through independent actions in each lattice direction. These techniques are often referred to as *link-wise* because they operate on “links” that connect the *boundary nodes* with the wall along with the discrete lattice directions. On a given link, they do not require any information from other nodal populations to reconstruct the unknown. The *link-wise* approaches have been generalized by the multireflection family of methods (MR) [8,13,20,21]. The branch of the MR characterized by linear interpolations is called LI [20]. Formally, both MR and LI are families of an infinite number of schemes that include most of the existing *linkwise* methods.

A subset of the *linkwise* group consists of techniques inspired by the *half-way bounce-back* (HW) rule [6,7] and commonly referred to as *interpolated bounceback* in recent literature [15,22–24]. The most common HW extension to treat curved boundary conditions is the Bouzidi, Firdaouss, and Lallemand method (BFL) [25]. The (linear) BFL additionally employs the populations in an adjacent layer to the boundary nodes to carry out interpolations dependent on the wall position. The boundary node-wall distance impacts both the

*francesco.marson@unige.ch; marson.francesco@gmail.com

interpolation coefficients and the populations involved in the interpolation scheme. In practice, the method is constituted by two subschemes (often denoted ULI and DLI [20]) that are alternatively applied depending on the distance between the wall and the boundary node. In the present article, we call *fragmented* methods with this characteristic. On the contrary, we use the term “*unified*” to refer to the monolithic algorithms where the wall position only determines the interpolation coefficients but not the interpolation scheme. Two years after the proposition of the BFL, Yu *et al.* [26] proposed a scheme (YLI) that can be considered as a *unified* version of the linear BFL, given that it uses the same populations as the BFL to perform the interpolation. Both methods are part of the LI family.

As previously mentioned, the LI is generalized and extended [8,13,20] by the multireflection (MR) methods of parabolic accuracy, featuring exact modeling of the grid-rotated parabolic profiles and quasianalytical accuracy in laminar flow around obstacles [11]. Using an appropriately parametrized collision model [11,20], the MR assures viscosity-independent accuracy of the steady-state velocity profiles. The MGLI method [20] makes this feature available with the LI methods, including the BFL and YLI schemes, thanks to local post-collision correction; this correction vanishes in one, simplest MGLI member called (central-linear) CLI scheme. On the contrary to the standard YLI, its MGLI counterpart does reduce to HW for boundary located between two nodes. MGLI and MR have been recently applied to various complex applications such as porous media [3,11] and finite Knudsen numbers applications [27–29], a fact that demonstrates the flexibility of the approach provided by its robust mathematical framework. Yet, LI/MGLI and MR methods share the drawback of not being local, needing at least a second layer of nodes to operate (a third layer is involved in the case of MR).

In the past two decades, few attempts to create local interpolated bounce-back schemes have been proposed [15–18,20]. A local version of LI was originally proposed to deal with corners using a first-order in time approximation in Ref. [20]. In fact, in the case of LI, one can reduce the access to the sole first layer of nodes by taking the previous time steps solution. This procedure is exact and automatic in the steady-state formulation [13]. This idea was resumed by Zhao and Yong (ZY) [16] that proposed a local version of the BFL method. In the same article [16], they also show, through a formal Maxwell’s iteration procedure, that the scheme is second-order accurate under diffusive scaling hypothesis. This boundary condition has been further validated in references [30,31] and developed in Ref. [32] to cancel the *viscosity dependent* errors. The ZY method has been tested by Peng *et al.* in Refs. [22,33]. Just like the original paper, they report second-order convergence and accuracy similar to the BFL.

The remaining local *interpolated bounce-back* methods [15,17,18] follow a different approach introduced by Chun and Ladd [15]. First, they reconstruct the boundary populations using the wall velocity and a constant approximation for the density. Then they use an approximated version of the nonequilibrium bounce-back of Zou and He (see Ref. [34]). However, Chun’s and Ladd’s method (CL) is not strictly local because, in some situations, it requires information from the

second layer of nodes. In the wake of Chun and Ladd, in recent years, two new local boundary conditions have been proposed: Tao *et al.* (NELI–ULT) [17] and Liu *et al.* [18].

Among the first local *linkwise* techniques, the Filippova and Hanel (FH) [35,36] can be singled out. The FH belongs to the family of *ghost methods* [9], also known as *extrapolation methods* [37] or *fictional equilibrium methods* [38], that uses additional fictitious nodes on the solid side of the boundary together with extrapolations to reconstruct the unknown populations. In FH the ghost node used for the interpolation is built guessing a velocity beyond the wall with an extrapolation of the boundary velocity. Unfortunately, the FH method has known stability issues, solved by Mei, Li, and Shyy, but sacrificing the locality of the method [9,39].

Junk and Yang (JY) [14] proposed a *single-node* boundary condition based on a correction of the half-way bounce-back scheme. To perform the correction, it is necessary to solve a linear system on each node to ensure the compliance of the numerical result with the expected Navier-Stokes solution. For this reason, it cannot be considered *linkwise*. Besides, the resolution of the linear systems adds a layer of complexity to the implementation. This approach leads to an almost local mass conservative boundary condition that shows second-order convergence for the velocity. The method has been extensively tested by Yang [40] that concluded it has comparable or better accuracy of the BFL and FH methods. Nevertheless, Nash *et al.* reported in Ref. [41] poor stability properties for the JY method.

It is worth mentioning two other local non-*linkwise* methodologies. The partially saturated bounce-back (PSBB) [42] is a local method that can be interpreted as an improved full-way bounce back (i.e., the bounce-back version based on modified collision inherited from lattice gas automata [43,44]). The PSBB uses the fluid fraction in the boundaries cells to operate a mixed fluid-solid collision [9,42]. The PSBB shows good mass conservation and allows for a smooth transition between solid and fluid nodes in the case of moving objects. Moreover, it does not require the exact knowledge of the surface shape: this is particularly suitable for porous media applications. However, it can turn into a disadvantage if the goal is to guarantee an exact *no-slip condition* because the knowledge fluid fraction is not sufficient to “know” the boundary position and orientation. Therefore, this method cannot be considered second-order accurate. Also, it requires an additional computation step if the fluid fraction of boundary nodes needs to be computed knowing the geometrical shape of the wall. Furthermore, Chen *et al.* comparing different boundary conditions in Ref. [45] reported a low accuracy in the computation of the cylinder drag when using the PSBB. From the algorithmic point of view, the PSBB cannot be used to represent thin shells because this method constrains the user to allocate the solid nodes in the simulation.

We finally mention the local second-order boundary (LSOB) method of Ginzburg and d’Humières [10]. Like the parabolic MR, this method is based on a precise computation of the boundary nodes according to the Chapman-Enskog expansion to relate macroscopic fields such as density and velocity with the LBM mesoscopic populations. In contrast with MR, LSOB is not linkwise but a single-node technique. The LSOB is a high-fidelity third-order accurate local method

TABLE I. Summary of acronyms and boundary condition methods threaded in the introduction. (*) Applying the special treatment for corners, one can (also) recover the ZY method. (★) The CL method is technically single node only in presence of narrow gaps.

Method [reference]	Single node	Linkwise	$\geq 2^\circ$ order	Mass conservative	Year	Authors
HW [6,7]	✓	✓	×	✓	1994	Ginzburg and Adler/Ladd
LSOB [10,19]	✓	×	✓	×	1996	Ginzburg, d'Humières, Silva
FH [35]	✓	✓	✓	×	1997	Filippova and Hänel
PSBB [42]	✓	×	×	✓	1998	Noble and Trozynski
BFL (ULI/DLI) [25]	×	✓	✓	×	2001	Bouzidi, Firdaouss, Lallemand
YLI [26]	×	✓	✓	×	2003	Yu, Mei, Shyy
MR/MGLI/(C)LI [8,20]	×✓(*)	✓	✓	×	2003	Ginzburg, Verhaeghe, d'Humières
JY [14]	✓	×	✓	✓	2005	Junk and Yang
CL [15]	×✓(★)	✓	✓	×	2007	Chun and Ladd
ZY [16]	✓	✓	✓	×	2017	Zhao and Yong
ELI-ULT [17]	✓	✓	✓	×	2018	Tao, He, Chen, Yan, Huang

mainly intended for laminar flows. Though, its implementation and parametrization are lattice and problem-dependent [19].

Despite the existence of the single-node boundary conditions that we have reviewed and summarized in Table I, further research is needed to make local boundary conditions appealing in terms of accuracy and simplicity of the implementation. Furthermore, the interrelation between the existing local boundary methods should be clarified. To this end, in the present article, we develop a framework to generalize interpolated bounce-back schemes, including the CL, Tao, Liu, ZY local methods, and the well-established BFL, YLI, and CLI methods. Within this framework, we herein develop a family of boundary conditions with the aim to improve the compactness of the interpolation range and the accuracy of the nonequilibrium approximation adopted in the CL, Tao, and Liu methods.

This article is structured in the following way. To begin with, the LBM and the interpolated bounce-back methods are introduced respectively in Secs. II A and II B. Then, the general description of the local ELI is presented in Sec. III and the procedure to compute approximated populations located at the wall is explained in Sec. III A. The following Sec. IV, deals with the numerical analysis of the scheme. More specifically, Sec. IV A introduces the generalized description of linkwise interpolations at the boundary nodes and Sec. IV B shows the parametrization procedure of the schemes. More pragmatically Sec. V supply the values of the coefficients for different variants of the ELI schemes (Sec. V A) and provides indications for the implementation (Sec. V B). Finally, the implementation in the open-source software PALABOS [46] of the ELI is verified for three configurations where the analytical solution is known. Namely, the steady cylindrical Couette flow in Sec. VI A, the impulsively started unsteady Couette flow in Sec. VI B, and the Jeffery's orbit in Sec. VI C.

In the appendices, we provide complementary information to deepen the discussion of the main text. Some additional formulas are provided in Appendix A, while Appendices B and C contain, respectively, the review of the diffusive scaling and Chapman-Enskog expansion, followed by the parametrization procedure in Appendix D. We finally provide some technical details regarding Jeffery's orbit test case in Appendix E.

II. NUMERICAL METHODOLOGY

A. The lattice Boltzmann method

The (force-free) Boltzmann equation (BE) [47–49]

$$\partial_t f + \partial_\alpha \xi_\alpha f = \mathcal{Q}_{\text{BE}}(f, f) \quad (1)$$

describes the space and time evolution of the probability distribution function $f(\mathbf{x}, \boldsymbol{\xi}, t)$ of finding a particle with velocity $\boldsymbol{\xi}$ at position \mathbf{x} and time t . The latter is subject to advection in the velocity space $\boldsymbol{\xi}$, as well as collision as illustrated by the Boltzmann's collision integral $\mathcal{Q}_{\text{BE}}(f, f)$ [50–53]. The complexity of Boltzmann's collision integral is the major obstacle to the solution and analysis of the equation. This is why $\mathcal{Q}_{\text{BE}}(f, f)$ is commonly approximated, with *relaxation toward equilibrium* models. One of the oldest and most successful relaxation models is the BGK operator that was formulated independently by Bhatnagar, Gross, Krook [54] and by Welander [55] (introduced in the LBM by Qian [56]).

In the LBM context, the BE (1) is first decomposed in a *finite* set of equations resulting from the velocity space discretization [57,58]. Those equations are known as the Discrete Velocity Boltzmann Equation (DVBE) and read as

$$\partial_t f_i + \partial_\alpha \xi_\alpha f_i = \mathcal{Q}_{\text{DVBE}}(f_i, f_i). \quad (2)$$

Similar to the BE, the DVBE expresses the time evolution of *discrete* probability distribution functions $f_i(\mathbf{x}, \boldsymbol{\xi}_i, t)$. But contrarily to the BE, the latter “populations” now propagate at *constant* velocity $\boldsymbol{\xi}_i$ with $i \in \{0, 1, \dots, Q\}$. Applying the method of the characteristics and either the eulerian or trapezoidal integration rule, to the left-hand side (LHS) and right-hand side (RHS) terms of the DVBE (2) respectively [9,59], one ends up with the lattice Boltzmann equation (LBE) [60,61] that is the cornerstone of LBMs,

$$\text{expl.euler: } f_i(\mathbf{x} + \mathbf{c}_i, t + 1) = f_i(\mathbf{x}, t) - \Omega^{\text{E}} f_i^{\text{neq}}, \quad (3a)$$

$$\text{trapezoidal: } f_i(\mathbf{x} + \mathbf{c}_i, t + 1) = f_i(\mathbf{x}, t) - \underbrace{\Omega f_i^{\text{neq}}}_{\mathcal{Q}_{\text{LBM}}}, \quad (3b)$$

where all the variables are now in lattice units [lu] ($f \rightarrow \hat{f}$, $\mathbf{x} \rightarrow \mathbf{x}$, $t \rightarrow t$) and populations has been rescaled in the trapezoidal case ($f_i \rightarrow \hat{f}_i$, $f_i^{\text{neq}} \rightarrow \hat{f}_i^{\text{neq}}$, see Appendix A 1)

to preserve the form of the equation yet gaining the second-order accuracy. \mathcal{Q}_{LBM} consists in a heuristic approximation of \mathcal{Q}_{BE} , and Ω is the (rescaled) relaxation parameter. f_i^{eq} and $f_i^{\text{neq}} = f_i - f_i^{\text{eq}}$ are the equilibrium and nonequilibrium populations respectively. In practice, the LBE (3) is solved through two successive steps. The local *collision* step [RHS of Eq. (3)] and the nonlocal Lagrangian *streaming* step [LHS of Eq. (3)]. Through the normalization of discrete velocities ($\mathbf{c}_i = \xi_i c_s$ with c_s the lattice constant), the streaming satisfies the on-grid condition that leads to an *exact* advection of populations from one grid node to another one [9]. To compute the collision term, one needs to derive equilibrium and nonequilibrium populations. $f_i^{\text{eq}} = f_i^{\text{eq}}$ are the discrete counterpart of the Maxwell-Boltzmann distribution [53]. One way to derive f_i^{eq} from the Maxwellian is to rely on the Gauss-Hermite quadrature [57,58].

Regarding collision models, one of the most popular is the BGK approximation [56] that leads to

$$\text{expl.euler} : \quad \Omega_{\text{BGK}}^{\text{E}} = \frac{1}{\bar{\tau}}, \quad f_i^{\text{neq}} = (f_i - f_{i,2}^{\text{eq}}), \quad (4)$$

$$\text{trapezoidal} : \quad \Omega_{\text{BGK}} = \frac{1}{\tau}, \quad f_i^{\text{neq}} = (f_i - f_{i,2}^{\text{eq}}), \quad (5)$$

where $\bar{\tau}$ is the relaxation time and $\tau = \bar{\tau} + 1/2$ is the redefined relaxation time in the trapezoidal integration case.

$$f_{i,2}^{\text{eq}} = w_i \rho \left[1 + \frac{c_{i\alpha_1} u_{\alpha_1}}{c_s^2} + \frac{u_{\alpha_1} u_{\alpha_2} (c_{i\alpha_1} c_{i\alpha_2} - c_s^2 \delta_{\alpha_1 \alpha_2})}{2c_s^4} \right] \quad (6)$$

is the discrete equilibrium up to the second-order, where $\alpha_i \in \{x_1, \dots, x_d\} \forall i$ and Einstein's summation rule is assumed.

The BGK collision model is easy to understand and implement, but it has several drawbacks. Concerning the bounce-back method, the coupling with the BGK collision model gives rise to a *second-order* error (related to the exact location of the wall) that is commonly referred to as *viscosity-dependent error* [7,8]. Among the other limitations, it can lead to numerical instabilities in the case of under resolved meshes (typically at high Reynolds numbers) and nonvanishing Mach numbers [9,37,62]. To overcome these issues, several extended collision models were proposed [63] with varying degrees of success [62]. Hereinafter, we will restrict ourselves to multi-relaxation-time (MRT) [64–66], focusing in particular on the two-relaxation-time (TRT) [21,67,68], because we will see that the latter is particularly interesting for boundary conditions, especially in the low Reynolds number regime.

The core idea of the MRT models is to carry out the relaxation collision process in the moment space. In other terms, from Q populations, Q moments are computed. The latter are (independently) relaxed toward their equilibrium values using different relaxation parameters. This method depends on many free parameters, though, which need to be handpicked through an adequate procedure [11,69].

a. TRT models. To reduce the number of relaxation rates still retaining one collision freedom, Ginzburg *et al.* proposed in Refs. [67,68] a TRT formulation of the MRT collision model (see also Refs. [13,20,21,70,71]). These TRT-LBMs independently relax even (symmetric) and odd (antisymmetric) moments and to each group assign an individual relaxation time: τ^+ and τ^- , respectively. Thanks to the fact that the lattice is usually symmetric ($\forall \mathbf{c}_i \exists -\mathbf{c}_i$), the symmetric and

antisymmetric moments can be associated with the symmetric and antisymmetric component of the populations. In this way, the TRT-LBM and the corresponding collision operator reads

$$f_i^{\pm}(\mathbf{x} + \mathbf{c}_i, t + 1) = f_i^{\pm}(\mathbf{x}, t) - \Omega_{\text{TRT}}^{\pm} f_i^{\pm \text{neq}}, \quad (7a)$$

$$\Omega_{\text{TRT}}^{\pm} = \frac{1}{\tau^{\pm}} = \frac{1}{\bar{\tau}^{\pm} + 1/2} = \frac{1}{\Lambda^{\pm} + 1/2}, \quad (7b)$$

where Λ^{\pm} is the standard notation to refer to $\bar{\tau}^{\pm}$. The symmetric and antisymmetric populations component reads

$$f_i^+ = \frac{f_i + f_{\bar{i}}}{2}, \quad f_i^- = \frac{f_i - f_{\bar{i}}}{2}, \quad f_i = f_i^+ + f_i^-, \quad (8)$$

where \bar{i} indicates the index associated with opposite direction, i.e., $\mathbf{c}_{\bar{i}} = -\mathbf{c}_i$. Interestingly, the TRT spatial behavior can be described by the *magic parameter* Λ that relates the two collision frequencies in the following way:

$$\Lambda = \Lambda^+ \Lambda^- = (\tau^+ - 1/2)(\tau^- - 1/2). \quad (9)$$

TRT-based collision models are particularly interesting for the bounce-back boundary condition. At steady state, for any determined value of Λ , the HW bounce-back condition is *viscosity-independent* [8], i.e., the wall location does not depend on the viscosity anymore. The latter feature is particularly critical for high-viscosity flows and for the acceleration to steady state. Moreover, Λ controls the exact position of the wall and, in the case of the Poiseuille flow, $\Lambda = 3/16$ locates the boundary exactly at midway between solid and boundary nodes [7,8,11]. One may notice that while in the TRT model Λ can be kept constant, on the contrary, in the BGK we have $\Lambda \propto \nu^2$. Indeed, the BGK can be seen as a subset of the TRT models constrained to $\tau^+ = \tau^-$. Unfortunately, the TRT does not lead automatically to viscosity independent error interpolated bounce-back methods. These methods need to be *parametrized* with a correction that needs to be added to the interpolation, as it has been done [20] from the LI method to its MGLI counterpart.

B. Geometrical interpretation of the interpolated bounce-back methods

The purpose of boundary algorithms is to reconstruct missing populations on nodes next to the wall (*boundary nodes*), after the streaming step. On the *boundary nodes* F , the unknown population are those associated with discrete velocities \mathbf{c}_i that “leave” the wall (see Fig. 1). We call such populations “*incoming to fluid*” and denote them with index i , while we call “*outgoing from fluid*” and denote with the index \bar{i} the others [37]. The main idea of the interpolated bounce-back methods (IBB) is to perform a one-dimensional polynomial interpolation of the known population close to the boundaries along with the discrete directions of the lattice (links directions) to recover the unknown *incoming* populations at the *boundary nodes*. For resting boundaries, we can formalize this general idea in mathematical terms writing

$$f_i(\mathbf{x}_F, t + 1) = \sum_j a_j f_i^*(\mathbf{x}_j, t) + \sum_k a_k f_{\bar{i}}^*(\mathbf{x}_k, t) + K, \quad (10a)$$

where $f^* = f - \Omega f^{\text{neq}}$ is a post-collision population, K is a hypothetical correction, the symbol a denotes the

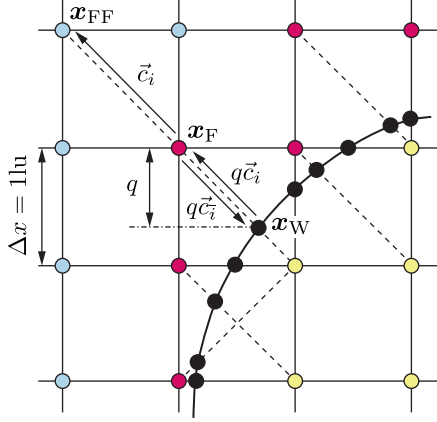


FIG. 1. 2D representation of the boundary nodes, normalized distance q , discrete lattice velocities \vec{c}_i , \vec{c}_i , links (dashed segments), and locations of boundaries at the intersections with links (\bullet). Δx is the space step.

interpolation coefficients, \mathbf{x} is an interpolation point and t is the current iteration. In practice, for the linear case and referring to Fig. 1, the previous formula generally reduces to

$$f_i(\mathbf{x}_F, t+1) = a_1 f_i^*(\mathbf{x}_{FF}, t) + a_2 f_i^*(\mathbf{x}_F, t) + a_3 f_i^*(\mathbf{x}_F, t) + K. \quad (10b)$$

Equations (10) represent a generic formulation of the interpolated-bounceback approach. To derive a specific method, it is necessary to specify the expressions of the interpolation coefficients. To this end, two viable solutions exist. The first one consists of writing closure relations by exploiting the macroscopic *no-slip* condition [7,8,20,21]. In practice, Eqs. (10) are expressed through the parabolic-accurate Chapman-Enskog population solution around the macroscopic variables and fitted to a formal Taylor expansion of the no-slip condition. The second solution relies on a mesoscopic, geometrical approach proposed by Bouzidi *et al.* [25]. In this case, the idea is to use the bounce-back rule, understood as a modification to the streaming step, to compute the interpolation coefficients. Roughly speaking, the bounce-back operator modifies the streaming operator from a simple translation in space to a translation-reflection-translation. The populations subjected to the bounce-back, during the translation, are reflected when they encounter the wall. The interpolation coefficients are those that allow to geometrically compute the unknown either at time step $t+1$ or at its virtual off-lattice post-collision state at time t .

To illustrate this concept we consider the BFL algorithm [25]. For the linear BFL algorithm, Eq. (10b) becomes

$$f_i^{t+1}(\mathbf{x}_F) = \underbrace{\frac{a_1}{2q}}_{a_1} f_i^*(\mathbf{x}_F) + \underbrace{(1-2q)}_{a_2} f_i^*(\mathbf{x}_{FF}) \quad q < 0.5 \quad (11a)$$

$$f_i^{t+1}(\mathbf{x}_F) = \underbrace{\frac{1}{2q}}_{a_1} f_i^*(\mathbf{x}_F) + \underbrace{\frac{2q-1}{2q}}_{a_3} f_i^*(\mathbf{x}_F) \quad q \geq 0.5 \quad (11b)$$

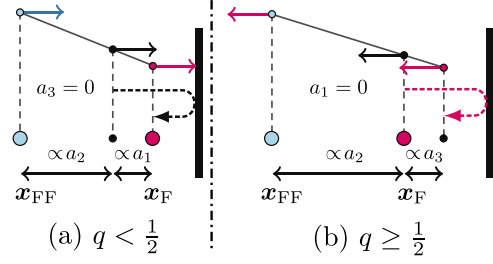


FIG. 2. 1D linkwise representation of bounce-back procedure in the BFL method: (left) $q < 1/2$ and (right) $q \geq 1/2$. The coefficients a_1, a_2, a_3 and the populations are defined in Eqs. (11). The arrows represent the populations and their color is related to the color of the node from which they depart at time t after the collision: light blue for node FF, magenta for node F, black for an off-lattice position. The dashed curved arrows represent the bounce-back rule. (a) the bounce-back rule is applied after the interpolation. (b) the bounce-back rule is applied before the interpolation.

where q denotes the distance of the boundary node F from the wall, normalized by the norm of the discrete velocity $\|\mathbf{c}_i\| = \|\mathbf{x}_{FF} - \mathbf{x}_F\|$. As shown in Fig. 2, in the IBB methods, populations can be thought of as lumped mass elements moving according to their discrete lattice velocities \mathbf{c}_i . During the streaming step, each population undergoes either the free streaming (along a straight line) or the bounce-back streaming (in the event of a wall encounter). In the latter case, the populations revert their streaming direction before completing their trajectory of the length of $\|\mathbf{c}_i\|$. When $q < 1/2$ [Fig. 2(a)], the interpolation is carried out when all populations are at the time step t in their post-collision state. In this case, the target location of interpolation is the former position of $f_i^{t+1}(\mathbf{x}_F)$ before the bounce-back streaming step (represented by the dashed curved arrow in the figure). On the contrary, when $q \geq 1/2$ [Fig. 2(b)], the interpolation factors must be computed after the streaming procedure. As a consequence, either the streaming or the bounce-back rule (represented by the dashed magenta arrow in the figure) is applied to each population at time step t (post-collision state). After that, the interpolation is carried out at time step $t+1$, as shown in Fig. 2(b).

In the present work, we propose to introduce a new metric for the interpolation in the IBB that allows for a more intuitive and uniform interpolation procedure. In effect, the expression of the interpolation procedure as a normalized distance from the wall can help to simplify and generalize the interpolation procedure. We discuss this topic in Sec. IV A. As a further step, we then derive and examine ELI closure relations following [13,20] in Sec. IV B.

III. THE NEW ELI SCHEME

To design local linkwise BCs, one must discard the *nonlocal* contribution $f^*(\mathbf{x}_{FF})$ that appears in Eqs. (10b) and (11). From the algorithmic point of view, one could think to save the other population at node F before the streaming. Then, to apply the boundary method after streaming. Unfortunately, this procedure leads only to an “algorithmic” locality that presents an issue: it does not allow to describe corners or narrow gaps (where a second wall is located between the nodes F and FF)

without introducing a special treatment of these cases [15]. To get rid of the unwanted $f^*(\mathbf{x}_{FF})$ population, yet maintaining the *linkwise* nature of the method, two approaches have been proposed. The first one, initially suggested by Ginzburg *et al.* [20] as a solution to corner problems, has been proposed as an independent method by Zhao *et al.* [16,30] and is based on the following first-order in time approximation

$$f_i^*(\mathbf{x}_{FF}) = f_i^{t+1}(\mathbf{x}_F) \approx f_i(\mathbf{x}_F). \quad (12)$$

Equation (12) can be used on the linear “multireflection” methods (MGLI) [13,20], getting in this way other single-node schemes (that have the advantage of being viscosity independent).

The second one, was introduced by Chun and Ladd [15], further developed by Tao *et al.* [17] and also improved by the present article. It consists in building virtual (approximated) populations located at the wall position \mathbf{x}_W . In the proposition of Tao *et al.* [17], only the population $\tilde{f}_i^{t+1}(\mathbf{x}_W)$ was introduced in Eq. (10b), where the cap “ \sim ” indicates an approximated value. Hereinafter, we propose a Enhanced Local Interpolated bounce-back method (ELI) which additionally accounts for the population $\tilde{f}_i^*(\mathbf{x}_W)$ hence, extending Eq. (10b) with the following formula:

$$\text{ELI} \left\{ \begin{aligned} f_i(\mathbf{x}_F, t+1) &= a_1 \tilde{f}_i^*(\mathbf{x}_{FF}) + \\ &+ a_2 \underbrace{\left(f_i^*(\mathbf{x}_F) + 2f_i^{\text{eq}^-}(\mathbf{x}_W) \right)}_{\text{HW [6, 7]}} + \\ &+ a_3 f_i^*(\mathbf{x}_F) + a_4 \underbrace{\tilde{f}_i(\mathbf{x}_W, t+1)}_{\text{by Tao et al. [17]}} + \\ &+ a_5 \underbrace{\tilde{f}_i^*(\mathbf{x}_W)}_{\text{new ELI}} - K^- \underbrace{\frac{f_i^{\text{neq}^-}(\mathbf{x}_F)}{\tau^-}}_{\text{optional sec. IV B}} \end{aligned} \right. \quad (13)$$

which represents the scheme underlying the new ELI method. In the previous formula, the expression of the antisymmetric component of equilibrium population at the wall reads $f_i^{\text{eq}^-}(\mathbf{x}_W) = w_i \rho c_i \cdot \mathbf{u}_w / c_s^2$. It is nonzero when the boundary moves with respect to the lattice.

The wall-populations remain to be determined: Sec. III A will reveal their expressions. The numerical analysis discussed in Sec. IV B will show that the ELI method represented by Eq. (13) give rise to an infinite number of similar accuracy schemes controlled by two free-tunable coefficients, namely a_2 and a_3 . Therefore, it is necessary to establish a proper methodology to specify the interpolation coefficients (Secs. IV A and V A) and the correction constant K^- necessary to parametrize the method, i.e., make its accuracy viscosity independent in the steady state (Sec. IV B). One may also note here that the model proposed by Tao *et al.* [17] directly follows from the ELI Eq. (13) with an appropriate choice of coefficients; for this reason, it is denoted with the acronym NELI-ULT in the present article.

A. Approximation of the populations at the wall

The wall populations $\tilde{f}_i(\mathbf{x}_W, t+1)$ and $\tilde{f}_i^*(\mathbf{x}_W, t)$ appearing in Eq. (13) are computed using a separate estimation for the equilibrium and the nonequilibrium, as

$$\tilde{f}_i^*(\mathbf{x}_W, t) \stackrel{\text{def}}{=} \tilde{f}_i^{\text{eq}}(\mathbf{x}_W, t) + (1 - \Omega) \tilde{f}_i^{\text{neq}}(\mathbf{x}_W, t), \quad (14a)$$

$$\tilde{f}_i(\mathbf{x}_W, t+1) \stackrel{\text{def}}{=} \tilde{f}_i^{\text{eq}}(\mathbf{x}_W, t+1) + \tilde{f}_i^{\text{neq}}(\mathbf{x}_W, t+1). \quad (14b)$$

The specific equilibrium and nonequilibrium approximations will be explained in the next paragraphs.

a. Equilibrium wall populations. In the approach introduced by Chun in Ref. [15], the fundamental idea to realize a single-node IBB is to exploit the knowledge of the boundary velocity to rebuild some *virtual populations* at the boundary location. This approach consists of using the boundary velocity and an estimation of the density at the boundary to rebuild the equilibrium population. In Ref. [15], it has been shown that for a “slow” flow the approximation

$$\tilde{f}_i^{\text{eq}}(\mathbf{x}_W, t+1) \approx f_i^{\text{eq}}[\rho(\mathbf{x}_F, t), \mathbf{u}(\mathbf{x}_W, t+1)] \quad (15a)$$

is second-order accurate. It is possible to express the previous equation in terms of symmetric and antisymmetric components

$$\tilde{f}_i^{\text{eq}}(\mathbf{x}_W, t+1) \approx f_i^{\text{eq}^+}[\rho(\mathbf{x}_F, t), \mathbf{u}(\mathbf{x}_{[F,W]}, t+1)] + f_i^{\text{eq}^-}[\rho(\mathbf{x}_F, t), \mathbf{u}(\mathbf{x}_W, t+1)], \quad (15b)$$

where we added the possibility (to be investigated) to use \mathbf{u}_F in place of \mathbf{u}_W in the symmetric component: even if this can be counter-intuitive, it could help to improve the closure relation of the boundary condition discussed in Sec. IV B and Appendix D, in the case of nonlinear equilibrium. We can also apply the same approximation at the previous time step:

$$\tilde{f}_i^{\text{eq}}(\mathbf{x}_W, t) \approx f_i^{\text{eq}^+}[\rho(\mathbf{x}_F, t), \mathbf{u}(\mathbf{x}_{[F,W]}, t)] + f_i^{\text{eq}^-}[\rho(\mathbf{x}_F, t), \mathbf{u}(\mathbf{x}_W, t)]. \quad (15c)$$

One may note that in general $\mathbf{x}_W(t) \neq \mathbf{x}_W(t+1)$ and $\mathbf{u}(\mathbf{x}_W(t)) \neq \mathbf{u}(\mathbf{x}_W(t+1))$, but their actual expressions depend on the time advance scheme of the wall (e.g., explicit euler, implicit euler, etc.). Further, even if we show in Eqs. (13), (14), and (15) that the wall populations are computed at integer time steps, this is not mandatory. A proper *parametrization* of the schemes can handle the noninteger time step that best suits the wall-advancing scheme. We plan to further investigate this point in a future work together with the time-dependent analysis. Anyway, if $\Delta \mathbf{u}_w \ll \mathbf{u}_w$ it is assumed that one can set $\mathbf{u}[\mathbf{x}_W(t)] \approx \mathbf{u}[\mathbf{x}_W(t+1)]$ wall-advancing.

b. Nonequilibrium wall populations. Regarding the approximation of the *nonequilibrium* component at the wall $\tilde{f}_i^{\text{neq}}(\mathbf{x}_W, t+1)$ we can use an *approximated nonequilibrium bounce-back* [15,17,18]. This is a first-order approximation of the *nonequilibrium bounce-back* method of Zou and He [34] and it leads to the following second-order accurate approximation:

$$\tilde{f}_i^{\text{neq}}(\mathbf{x}_W, t+1) \approx f_i^{\text{neq}}(\mathbf{x}_F, t). \quad (16)$$

As demonstrated in Ref. [15] the reason why the approximated nonequilibrium bounce-back leads to a second-order accurate boundary condition resides in the fact that the

nonequilibrium component is a second-order correction over the equilibrium. This fact allows for a second-order approximation with an only first-order approximation of the nonequilibrium part. If one makes explicit the effect of this assumption on the symmetric $f_i^+ = (f_i + \bar{f}_i)/2$ and antisymmetric $f_i^- = (f_i - \bar{f}_i)/2$ components of f_i , Eq. (16) implies

$$N : f_i^{\text{neq}+}(\mathbf{x}_W) \approx f_i^{\text{neq}+}(\mathbf{x}_F), \quad (17a)$$

$$f_i^{\text{neq}-}(\mathbf{x}_W) \approx -f_i^{\text{neq}-}(\mathbf{x}_F). \quad (17b)$$

The ELI schemes using Eq. (17) are not consistent with respect to symmetry argument, therefore they are referred to as *nonsymmetric enhanced local interpolation* (NELI).

An alternative choice is to simply neglect the variation of the nonequilibrium components between \mathbf{x}_F and \mathbf{x}_W :

$$S : f_i^{\text{neq}+}(\mathbf{x}_W) \approx f_i^{\text{neq}+}(\mathbf{x}_F), \quad (18a)$$

$$f_i^{\text{neq}-}(\mathbf{x}_W) \approx f_i^{\text{neq}-}(\mathbf{x}_F). \quad (18b)$$

We refer to the respective ELI variants as *symmetric enhanced local interpolation* (SELI).

Finally, taking the average of the two previous approaches one can find

$$C = \frac{N+S}{2}, \quad (19)$$

such that

$$C : f_i^{\text{neq}+}(\mathbf{x}_W) \approx f_i^{\text{neq}+}(\mathbf{x}_F), \quad (20a)$$

$$f_i^{\text{neq}-}(\mathbf{x}_W) = 0. \quad (20b)$$

In this case, we refer to the ELI schemes as *central enhanced local interpolation* (CELI).

IV. NUMERICAL ANALYSIS

In this section, first, we develop a generalized geometrical procedure for computing suitable interpolation coefficients (Sec. IV A). Then we present the numerical analysis/parametrization of the ELI scheme (Sec. IV B). It should be remarked right from the beginning that an infinite number of possible ELI schemes is formally possible. This is analogous to what happens for MR and MGLI

methods [20]. The analysis of Sec. IV B will show that one can freely pick two parameters in Eq. (13) if K^- is consequently chosen. From this point of view, we can interpret the generalized procedure delineated in the next Sec. IV A as a proper way of choosing the free parameters in a geometrically meaningful way.

A. Generalized geometrical computation of interpolation coefficients

To obtain a more uniform picture of the interpolation procedure described in Sec. II B, we propose to express the populations of the IBB methods in their *precollision* state at time $t+1$ in a similar fashion of the case $q \geq 1/2$ of the BFL method (Fig. 2). To extend this description to any scheme and value of q , we introduce a signed normalized distance from the wall s at time $t+1$. At the time $t+1$ some population has been streamed following the free stream rule, whilst others near the wall have been streamed using the bounce-back rule described in Sec. II B and Fig. 2(b). In this condition the generalized coordinate s reads

$$s[f_{\mathcal{I}}(\mathbf{x}, t+1)] \stackrel{\text{def}}{=} \frac{(\mathbf{x} - \mathbf{x}_W) \cdot \mathbf{c}_{\mathcal{I}}}{\|\mathbf{c}_{\mathcal{I}}\|} \quad \forall \mathcal{I} \in \{i, \bar{i}\}, \quad (21)$$

where \mathbf{x} is the coordinate of the population $f_{\mathcal{I}}$ after the streaming/bounce-back step. From the definition of the generalized coordinate s one can see that if $\mathbf{c}_{\mathcal{I}}(f_{\mathcal{I}}) = \mathbf{c}_i$ then the population (at $t+1$) is *incoming* and s is positive, otherwise the population is *outgoing* and s is negative.

The coordinate s turns out to be a simple yet effective tool to describe and compare linkwise boundary conditions. Using Eq. (21), we can define a set of simple rules to move from the \mathbf{x} coordinate metric to the s coordinate metric:

$$f_i(\mathbf{x}_F, t+1) \equiv f(s=q), \quad (22a)$$

$$f_i^*(\mathbf{x}_F, t) = f_i(\mathbf{x}_{FF}, t+1) \equiv f(s=q+1), \quad (22b)$$

$$f_{\bar{i}}^*(\mathbf{x}_F, t) \equiv f(s=-q+1), \quad (22c)$$

$$f_{\bar{i}}^*(\mathbf{x}_{FF}, t) = \bar{f}_{\bar{i}}(\mathbf{x}_F, t+1) \equiv f(s=-q), \quad (22d)$$

$$f_i^*(\mathbf{x}_W, t) \equiv f(s=1), \quad (22e)$$

$$f_i(\mathbf{x}_W, t+1) \equiv f(s=0), \quad (22f)$$

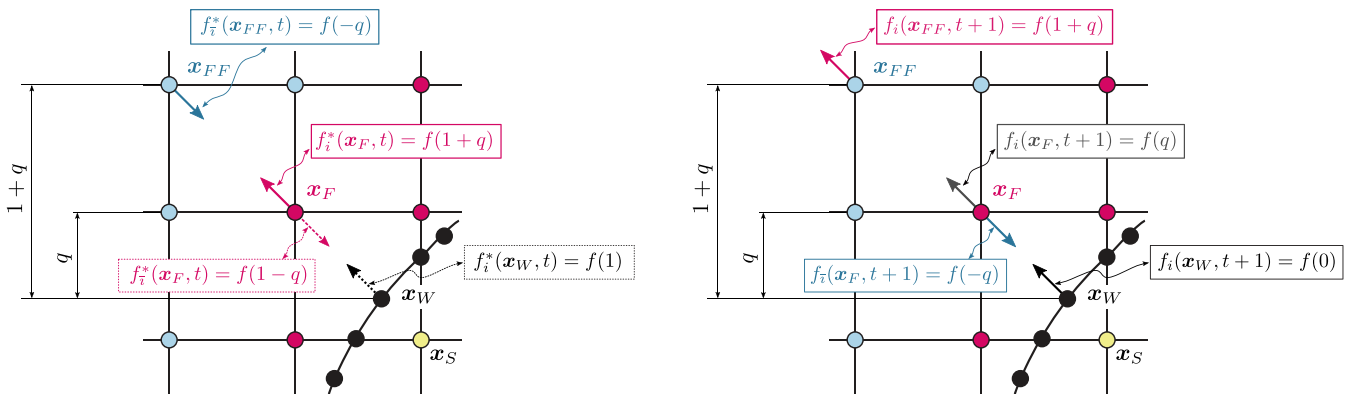


FIG. 3. Equivalences of the representation of population (arrows) through the standard space-time coordinates (LHS of the equivalences) and through the generalized coordinate (RHS of the equivalences). *On the left*: arrows represent populations at time t in their post-collision state. *On the right*: arrows represent populations at time $t+1$ in their precollision state.

TABLE II. Interpolation coefficients and parametrization constants for the ELI method variants to be used in Eq. (13).

	q	a_2	a_3	a_4	a_5	$N : K_1^-$	$N : K_2^-$	$S : K_1^-$	$S : K_2^-$	$C = \frac{1}{2}(N + S) : K_1^- = K_2^-$
ELI-UL	[0,1]	0	0	$1 - q$	q	$a_4 + \Lambda^-$	a_4	$a_5 - \Lambda^-$	a_5	$\frac{1}{2}(a_5 + a_4)$
ELI-ULT	[0,1]	0	$\frac{q}{1+q}$	$\frac{1}{1+q}$	0	$1 + a_4 \Lambda^-$	1	$a_4(q - \Lambda^-)$	$a_4 q$	$\frac{1}{2}(1 + a_4 q)$
ELI-UQ	[0,1]	1	0	$1 - 2q$	$-a_4$	a_4	a_4	$-a_4$	$-a_4$	0
ELI-FL(1)	$[0, \frac{1}{2}]$	$\frac{q}{1-q}$	0	$\frac{1-2q}{1-q}$	0	$a_4(1 + \Lambda^-)$	a_4	$-a_4 \Lambda^-$	0	$\frac{a_4}{2}$
ELI-FL(2)	$[\frac{1}{2}, 1]$	$\frac{1-q}{q}$	0	0	$\frac{2q-1}{q}$	$a_5 \Lambda^-$	0	$a_5(1 - \Lambda^-)$	a_5	$\frac{a_5}{2}$
ELI-FQ(1)	$[0, \frac{1}{2}]$					ELI-UQ				
ELI-FQ(2)	$[\frac{1}{2}, 1]$	$\frac{1-q}{2q^2}$	$\frac{1-3q+2q^2}{2q^2}$	0	$\frac{2q-1}{q^2}$	$a_3 + a_5 \Lambda^-$	a_3	$1 - a_2 - a_5 \Lambda^-$	$1 - a_2$	$\frac{1}{2}(1 + a_3 - a_2)$

which are graphically represented in Fig. 3. Equations (21) and (22) can be used to reinterpret the general ELI Eq. (13) in terms of the s coordinate (see Appendix A2). This change of reference system can be a useful tool for the implementation of linkwise methods because the s coordinates becomes a unique identifier for each interpolating population.

With the help of the coordinate s , it is now possible to generalize the formulas used in the BFL and the other IBB methods with the Sylvester-Lagrange polynomial interpolation formula [72,73]:

$$f(q, t + 1) = \sum_{j=0}^n a_j(s_j) f(s_j, t + 1), \quad (23)$$

where n is the interpolation order, j is the index of the interpolation point, and a_j are the interpolation coefficients given by

$$a_i = \prod_{\substack{0 \leq j \leq n \\ j \neq i}} \frac{q - s_j}{s_i - s_j}. \quad (24)$$

In the linear case the interpolation coefficients $a_j \in \{a_\alpha(s_\alpha), a_\beta(s_\beta)\}$ can be easily recovered from the values of $s_j \in \{s_\alpha, s_\beta\}$ in the following way:

$$a_\alpha(s_\alpha(q)) = 1 - \frac{q - s_\alpha}{s_\beta - s_\alpha}, \quad (25a)$$

$$a_\beta(s_\beta(q)) = \frac{q - s_\alpha}{s_\beta - s_\alpha}, \quad (25b)$$

$$s_\alpha < q < s_\beta. \quad (25c)$$

Equations (25) will be used to develop variants of the general ELI Eq. (13).

B. Parametrization of the schemes

With ‘‘parametrization of the schemes’’ we mean the procedure to cancel viscosity-dependent errors at steady state, determining the value of K^- appearing in the general ELI Eq. (13). The viscosity error is more critical in the regime of high viscosity and low Reynolds numbers, for this reason the main focus is the Stokes flow. In fact, in the case of high Reynolds numbers, LBM is generally limited to the *over-relaxation* regime ($\tau^+ \rightarrow 1/2$), where the viscosity-dependent errors are generally less important.

To each set of interpolation coefficients a_i (i.e., ELI variant) corresponds a different value for the parametrizing constant K^- . We will provide two possible values of K^- , K_1^-

and K_2^- , for each ELI variant. The specific values for K_1^- and K_2^- will be provided in Sec. VA together with the values of the interpolation coefficients (see in particular Table II). Here we summarize the main points of the parametrization procedure, for the detail please see also Appendix D. The steps of the analysis are the following:

- (1) Time Taylor expansion of the LHS of Eq. (13):

$$f_i(\mathbf{x}_F, t + 1) \approx f_i(\mathbf{x}_F, t) + \partial_t f_i(\mathbf{x}_F, t) + \partial_t^2 \frac{f_i(\mathbf{x}_F, t)}{2}. \quad (26)$$

- (2) Decomposition of populations in symmetric/antisymmetric and equilibrium/non-equilibrium components along the cut direction \bar{i} :

$$\begin{aligned} f_{\bar{i}} &= f_{\bar{i}}^{\text{eq}+} + f_{\bar{i}}^{\text{neq}+} - f_{\bar{i}}^{\text{eq}-} - f_{\bar{i}}^{\text{neq}-}, \\ f_{\bar{i}} &= f_{\bar{i}}^{\text{eq}+} + f_{\bar{i}}^{\text{neq}+} + f_{\bar{i}}^{\text{eq}-} + f_{\bar{i}}^{\text{neq}-}. \end{aligned} \quad (27)$$

- (3) Chapman-Eskog expansion of the nonequilibrium solution to TRT Eq. (7a) (see Appendix C), under the *diffusive scaling* hypothesis (see Appendix B1). Assuming the Einstein’s summation rule for α indexes, this allows to find the following expression for the nonequilibrium:

$$\begin{aligned} f_{\bar{i}}^{\text{neq}\pm} &= \tau^\pm [-\partial_t f_{\bar{i}}^{\text{eq}\pm} - c_{i\alpha} \partial_\alpha f_{\bar{i}}^{\text{eq}\mp} \\ &\quad + \Lambda^\mp (c_{i\alpha} \partial_\alpha)^2 f_{\bar{i}}^{\text{eq}\pm}], \end{aligned} \quad (28)$$

which follows directly from Eq. (C9) assuming $f_i \approx f_{c,i}$ ($f_{c,i}$ is the reduced Chapman-Enskog population). Equation (28) is then used for analysis of Eq. (13) after applying the previous steps.

- (4) Injection of wall-nonequilibrium estimation [Sec. III A, Eq. (17) or Eq. (18) or Eq. (20)].

- (5) Rearrangement of the equation resulting from previous steps, gathering all the coefficients

$$\begin{aligned} &[\alpha^+ f_{\bar{i}}^{\text{eq}+} + \alpha^- f_{\bar{i}}^{\text{eq}-} + \tau^+ \partial_t f_{\bar{i}}^{\text{eq}+} + \tau^- \partial_t f_{\bar{i}}^{\text{eq}-} \\ &\quad + \beta^+ c_{\bar{i},\alpha} \partial_\alpha f_{\bar{i}}^{\text{eq}+} + \beta^- c_{\bar{i},\alpha} \partial_\alpha f_{\bar{i}}^{\text{eq}-} \\ &\quad + \nu^+ \partial_t^2 f_{\bar{i}}^{\text{eq}+} + \nu^- \partial_t^2 f_{\bar{i}}^{\text{eq}-} \\ &\quad + \theta^+ c_{\bar{i},\alpha} \partial_t \partial_\alpha f_{\bar{i}}^{\text{eq}+} + \theta^- c_{\bar{i},\alpha} \partial_t \partial_\alpha f_{\bar{i}}^{\text{eq}-} \\ &\quad + \gamma^+ (c_{\bar{i},\alpha} \partial_\alpha)^2 f_{\bar{i}}^{\text{eq}+} + \gamma^- (c_{\bar{i},\alpha} \partial_\alpha)^2 f_{\bar{i}}^{\text{eq}-}]_{\mathbf{x}_F}^t \\ &= [\alpha_W^+ f_{\bar{i}}^{\text{eq}+} + \alpha_W^- f_{\bar{i}}^{\text{eq}-}]_{\mathbf{x}_W}^{t+1}, \end{aligned} \quad (29)$$

where the greek-letter factors are linear combinations of the interpolation coefficients a_i , K^- , and Λ^\pm (check Appendix D for their expression at this stage). The terms crossed out

are neglected under the *diffusive scaling hypothesis* because they result to be of the third/fourth order with respect to the Knudsen number [for the details please see Appendices B 1 and C and in particular Eq. (C6)].

(6) First-order, as initial analysis, Taylor expansion of the last term of Eq. (29):

$$\alpha_W^- f_i^{\text{eq}-} \Big|_{x_W}^{t+1} \approx \alpha_W^- (f_i^{\text{eq}-} + \partial_t f_i^{\text{eq}-} + q c_{i,\alpha} \partial_\alpha f_i^{\text{eq}-}) \Big|_{x_F}^t. \quad (30)$$

The previous expansion allows to compare antisymmetric components of the RHS and LHS of the resulting equation. Considering the antisymmetric components up to the first-order, the comparison reads

$$\begin{aligned} \alpha^- f_i^{\text{eq}-} + \tau^- \partial_t f_i^{\text{eq}-} + \beta^- c_{i,\alpha} \partial_\alpha f_i^{\text{eq}-} \Big|_{x_F}^t \\ \approx \alpha_W^- (f_i^{\text{eq}-} + \partial_t f_i^{\text{eq}-} + q c_{i,\alpha} \partial_\alpha f_i^{\text{eq}-}) \Big|_{x_F}^t. \end{aligned} \quad (31)$$

To cancel zero and first order errors, it must hold

$$\alpha^- = \alpha_W^-, \quad \beta^- = q \alpha_W^- \quad (32a)$$

and

$$\tau^- = \alpha_W^-. \quad (32b)$$

The two relations of Eq. (32a) constrain the values of the interpolation coefficients in the following way:

$$a_4 = 1 + (a_3 - a_2 - 1)q, \quad (33a)$$

$$a_5 = a_2(-1 + q) + q - a_3(1 + q). \quad (33b)$$

Thus, only two of the four interpolation coefficients are linearly independent. Equation (32b) determines the time accuracy: the best time accuracy is achieved when Eq. (32b) is satisfied exactly. Nonetheless, it should be noted that Eq. (32b) has not general validity. It is a consequence of considering the wall populations defined at integer time steps, which is not the sole possibility (as discussed in Sec. III A). One could, for instance, chose to define them at the noninteger time t that best fits the wall-advancing scheme. We plan a more in-depth analysis of this fact for a future work. Please see Appendix D (step 6) for the details.

(7) Use of Eq. (33) to cancel the dependence of greek-letters coefficients from a_4 and a_5 . Their final expression is reported in Appendix D 2.

(8) Computation of K^- imposing two conditions on γ^- from Eq. (29). The first is that γ^- should not be a function of Λ^+ , to avoid the dependence of the closure relation on the viscous relaxation time when Λ is set. The second one is to have the same steady-state closure relation when Λ is set. We propose to satisfy the two conditions either using the LI/MGLI condition [20] (such that $\gamma^- = \Lambda \alpha^-$) or asking that K^- does not depend upon the collision model. For the detail please see Appendix D 3.

Although the derivation of K^- appears here in the context of the Chapman-Enskog approximation, it is exact for single-node boundary rules and should guarantee the exact scaling (viscosity-independent errors) at least for Stokes equilibrium, please see Refs. [13,70,74] for further extensions.

V. VARIANTS AND IMPLEMENTATION

A. ELI variants

The new generalized coordinate introduced by Eq. (21) is useful to develop variants of the general scheme proposed in Eq. (13), by specifying the interpolation coefficients and the parametrization constant K^- . We propose several variants of ELI in Table II using the following naming rule:

$$\begin{array}{ccc} K^- \in \{K_1^-, K_2^-\} & Y \in \{U, F\} & \\ \downarrow & \downarrow & \\ \mathbf{K} - \mathbf{XELI} - \mathbf{YZO} & \leftarrow \text{optional.} & \\ \uparrow & \uparrow & \\ X \in \{N, S, C\} & Z \in \{L, Q\} & \end{array}$$

K: parametrization constant, either K_1^- or K_2^- , to be used in Eq. (13) in place of K^- . Note that some methods of table II do not need the parametrization constant ($K^- = 0$) i.e., they are automatically viscosity independent at steady state.

X: nonequilibrium approximation at the wall, either nonsymmetric (N) Eq. (17), symmetric (S) Eq. (18) or central (C) Eq. (20).

Y: unified (U) or fragmented (F) method.

Z: linear (L) Eq. (25) or quadratic (Q) Eq. (24) interpolation. *N.B.* this should not be confused with the definition of *linear* interpolation schemes and *parabolic* interpolation schemes that refers instead to the *exactness* of the method [9].

O: optional specifier to distinguish variants having the same other letters. In practice it will be used only to distinguish ELI-ULT [17] from ELI-UL.

The expressions of the interpolation coefficients $a_{2,3,4,5}$ have been recovered converting the x coordinates in s coordinates with Eqs. (22) and then using Eqs. (24).

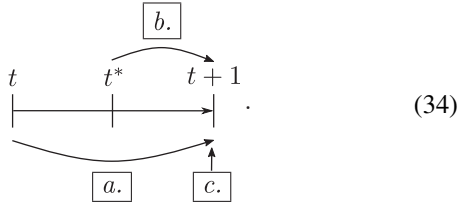
B. Implementation procedure

One of the following approaches can be chosen to implement the ELI schemes:

- Modified collision and streaming;
- Modified streaming;
- Modification of precollision populations.

If we consider that the time step changes after each *collide-stream* cycle and we call t^* the state of the algorithm after collision, then we can represent the algorithms of the

boundary condition as follows:



The implementation procedure is strictly related to the algorithmic structure of the LBM code (please see Refs. [75,76] for a summary of the possibilities). For this reason, a detailed discussion is outside the scope of the present article. Still, we briefly discuss these three alternatives in the following paragraphs.

a. Modified collision and streaming. It is the ideal implementation because it preserves the *algorithmic locality* and avoids unnecessary computations. Despite the simple logical procedure, it can be impractical and complex to implement in some codes. The reason resides in the fact that it requires modifying the collide and stream algorithm. The following two points need to be integrated into the same collide and stream procedure:

1. Apply a modified collide and stream using Eq. (13) to populations associated to \mathbf{c}_i that intersect the surface:

- (1) choose the variant from Table II;
- (2) compute density and velocity at the boundary nodes; in the forceless case,

$$\rho(\mathbf{x}_F, t) = \sum_{i=0}^{Q-1} f_i(\mathbf{x}_F, t), \quad \mathbf{u}(\mathbf{x}_F, t) = \frac{\sum_{i=0}^{Q-1} f_i(\mathbf{x}_F, t) \mathbf{c}_i}{\rho(\mathbf{x}_F, t)}; \quad (35)$$

in the presence of forcing, depending on the forcing scheme, the term $\mathbf{F}/2$ needs generally to be added to the expression of the velocity (\mathbf{F} being the body force); in addition, we note that the velocity should be computed using ρ_0 in place of ρ to have theoretically viscosity independent errors [3,8];

(3) compute the equilibrium at node F (time t) and at the wall using Eq. (15);

(4) compute nonequilibrium at the wall using Eq. (17), Eq.(18), or Eq. (20) (for parametrized method also compute $f_i^{\text{neq}^-}$);

(5) reconstruct wall populations using Eq. (14);

(6) collide populations at node F;

(7) compute $f_i(\mathbf{x}_F, t+1)$ and stream it in its location using Eq. (13).

2. Apply usual collide and stream to populations associated to \mathbf{c}_i that do not intersect the surface;

b. Modified streaming. It is a post-collision implementation very similar to the modified collision and streaming implementation. It applies at time step t , after performing the collision. It requires modifying the global stream procedure. With some LBM algorithms (e.g., with the *swap algorithm* [76]) it might not be convenient because it can also require store the precollision value at node F of some populations to recover the correct expression of the nonequilibrium estimation at the wall [for Eq. (17), Eq. (18), or Eq. (20)].

c. Modification of precollision populations. This approach is the most practical because it does not require modifying

the collide and stream. It applies at the beginning of the time step $t+1$. Unfortunately, this implementation can spoil the *algorithmic locality* using the *swap algorithm* [76]. Though, this does not happen in the case of the *double-population scheme*, for which it can be a convenient choice. For missing populations at the boundary nodes, do the following:

(1) choose the variant from Table II;

(2) recover previously computed $\rho(\mathbf{x}_F, t)$ and $\mathbf{u}(\mathbf{x}_F, t)$ using Eq. (35);

(3) compute the equilibrium at node F (time t) and at the wall using Eq. (15);

(4) compute nonequilibrium at the wall using Eq. (17), Eq. (18), or Eq. (20) (for parametrized method also compute $f_i^{\text{neq}^-}$):

(a) (only for *swap algorithm*) read the populations $f_i^*(\mathbf{x}_F, t)$ and $f_i^*(\mathbf{x}_F, t)$ in their new positions at time step $t+1$, i.e., $f_i(\mathbf{x}_{FF}, t+1)$ and $f_i(\mathbf{x}_S, t+1)$ (see Fig. 3);

(b) (only for *swap algorithm*) restore their precollision states [$f_i(\mathbf{x}_F, t)$ and $f_i(\mathbf{x}_F, t)$] either from previously stored values or applying an “inverse” collision ($f = f^* + \Omega f^{\text{eq}}$);

(c) compute the nonequilibrium component subtracting $f_{i,\bar{i}}^{\text{eq}}(\mathbf{x}_F, t)$ computed using the stored values of density and velocity (point 2);

(d) use Eq. (17), Eq. (18), or Eq. (20) (for parametrized method also compute $f_i^{\text{neq}^-}$);

(5) reconstruct wall populations using either Eq. (13) (*double-population scheme*) or the following modified equation that considers that the collide and the stream have already been applied (for *swap algorithm*):

$$\begin{aligned} f_i(\mathbf{x}_F, t+1) = & a_2[f_i(\mathbf{x}_S, t+1) + 2f_i^{\text{eq}^-}(\mathbf{x}_W)] \\ & + a_3 f_i(\mathbf{x}_{FF}, t+1) + a_4 \tilde{f}_i(\mathbf{x}_W, t+1) \\ & + a_5 f_i^*(\mathbf{x}_W) - K \frac{f_i^{\text{neq}^-}(\mathbf{x}_F)}{\tau^-}, \end{aligned} \quad (36)$$

where the term $f_i^{\text{eq}^-}(\mathbf{x}_W)$ is calculated using the density at the node F computed at the previous iteration (point 2) and \mathbf{x}_S is the first node beyond the boundary on along the link $\mathbf{x}_W - \mathbf{x}_F$.

In the case of a *double-population scheme* the above procedure turns out to be simplified and *algorithmically local*, given that the populations from the two different time steps are independently stored and accessible locally.

VI. RESULT AND DISCUSSION

The variants of the boundary condition method have been implemented for the D2Q9 and D3Q27 lattices, in the open-source library PALABOS [46] and validated with three test cases that do not involve LBM body forces, either with BGK or TRT collision models. We remark here that the presented BC rules apply directly in the presence of forcing term following [13,74].

The first test case is the steady-state cylindrical Couette flow. The purpose is to verify the steady-state behavior of the ELI variants. In particular, we check that the error of the parametrized versions is *viscosity-independent*. The mass-conservation of the schemes will also be investigated.

The second test case is the impulsively started Couette flow. In this case, the goal is to quantify the impact of the time-

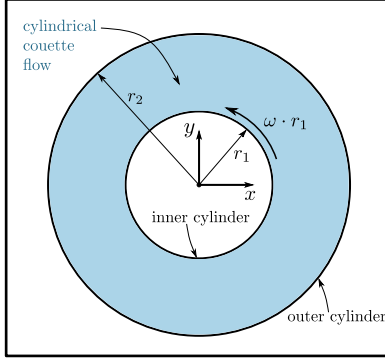


FIG. 4. Representation of computational domain. In blue, the intercylinders Couette flow. The external cylinder is resting, and the inner cylinder is moving with angular velocity ω .

dependent errors on the accuracy and compare the different variants.

The third test case is the Jeffery's orbit of a 3D prolate ellipsoid in a shear flow, which evaluates the capability of the ELI variants to properly simulate a rigid solid body immersed in viscous fluid flow.

A. Steady-state cylindrical Couette flow

The cylindrical Couette flow is a common benchmark to test the accuracy of curved boundary conditions. We implemented this test case using the D2Q9 and the D3Q27 lattices.

1. Description of the test case

In this test case, two coaxial cylinders are placed in the center of the simulation domain (Fig. 4). The cylinders axis is parallel to the z direction, along which the periodicity condition has been imposed. The inner cylinder of radius r_1 rotates with angular velocity

$$\omega_1 = u_\theta / r \quad \text{and} \quad u_\theta = \nu \text{Re} / (r_2 - r_1) \quad (37)$$

tangential velocity, while the outer of radius r_2 is at rest. The intercylinder distance $r_2 - r_1$ can be expressed using the cylinder ratio $\beta = r_1/r_2$ parameter as $r_1(1/\beta - 1)$.

The velocity flow inside the inner cylinder is linear if the flow is laminar, with a maximum tangential velocity $u_\theta = 1$ close to the inner cylinder and $u_\theta = 0$ in the center. Between the two cylinders, the solution for the fluid velocity at steady state is given by the cylindrical-Couette flow tangential velocity,

$$u_\theta = \frac{(r_1^2 - \beta^2 r^2)\omega_1}{(1 - \beta^2)r}, \quad (38)$$

where r is the radial distance from the axis of the cylinders.

The *root relative squared error* E_{rrs} (also known as relative ℓ^2 -norm error), defined as

$$E_{\text{rrs}}(u^*) = \sqrt{\frac{\sum_i^N [u^*(\mathbf{x}_i) - u_{\text{th}}^*(\mathbf{x}_i)]^2}{\sum_i^N u_{\text{th}}^{*2}(\mathbf{x}_i)}}, \quad (39)$$

is used to evaluate the convergence of computational error in the cylindrical Couette flow region (see Fig. 4), where \mathbf{x}_i is the coordinate of a lattice node, u^* is the computed dimensionless

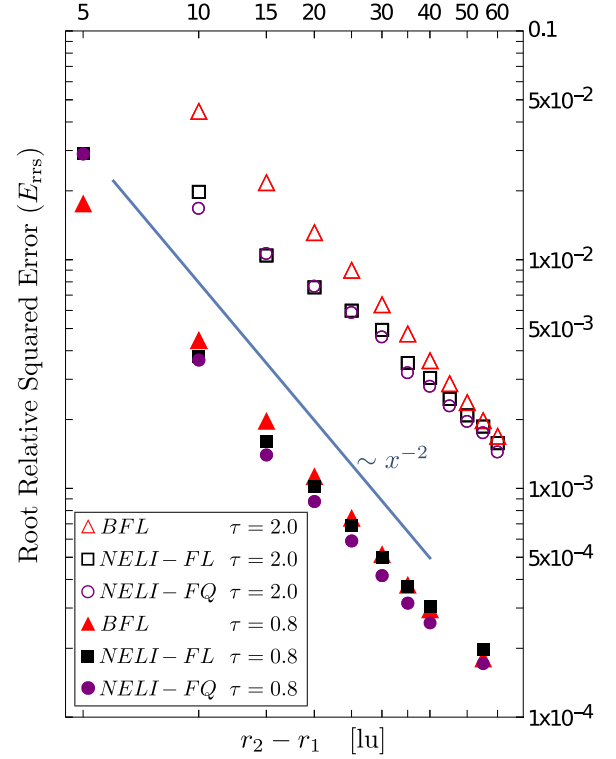


FIG. 5. E_{rrs} error of NELI-FL and NELI-FQ, and BFL methods against the resolution in lattice units [lu] with a D3Q27 lattice and TRT collision model ($\Lambda = 3/16$). The results are relative to steady-state condition for $\text{Re} = 1$.

macroscopic velocity norm and $u_{\text{th}}^* = u_\theta$ is the theoretical dimensionless velocity norm given by Eq. (38).

2. Analysis of the results

We performed different experiments to verify the sensitivity of the accuracy (measured with the E_{rrs}) to different parameters. Herein, we will focus on low Reynolds number flows $\text{Re} \ll 1$ simulated using a linear equilibrium for f^{eq} , i.e.,

$$f_{i,1}^{\text{eq}} = w_i \rho \left[1 + \frac{c_{i\alpha} u_\alpha}{c_s^2} \right], \quad (40)$$

where Einstein's summation rule is assumed for α indexes; the velocity u_α and the density ρ are computed using Eq. (35).

a. E_{rrs} convergence. We analyzed the error convergence under the *diffusive scaling* hypothesis. The goal is to verify the second-order convergence of the velocity field at steady state for the ELI variants and compare the results with other available methods, such as the BFL and its *single-node* alternative, the ZY method. Though, the burden of comparing the accuracy of the different methods in more detail is left to the following paragraphs. Here we consider the under-relaxed ($\tau^+ = 2.0$) and the over-relaxed ($\tau^+ = 0.8$) conditions using both BGK and TRT collision models either in combination with D2Q9 or D3Q27 lattices.

Figure 5 refers to the results for a D3Q27 lattice for the NELI schemes and the BFL method for both the under-relaxed ($\tau^+ = 2.0$) and over-relaxed ($\tau^+ = 0.8$) regimes using a TRT

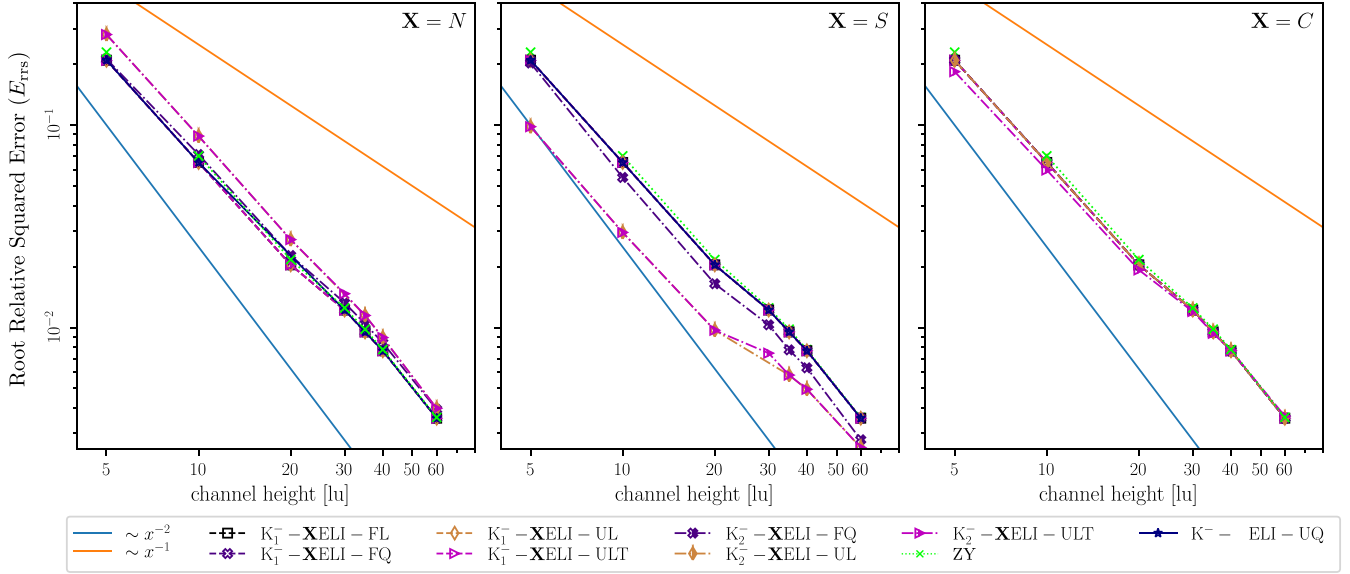


FIG. 6. E_{rms} error at steady state of ELI variants, and ZY methods for intercylinder distance $r_2 - r_1$ in lattice units [lu] (with $\beta = 1/2$). Results obtained using a D2Q9 lattice, BGK collision model, and linear equilibrium.

collision model with $\Lambda = 3/16$. In this case, the slope of the convergence is approximately of the second-order for all the considered variants and the BFL method.

Consider now the test presented by Fig. 6 for the under-relaxed regime (the most interesting for low Re flow). It has been performed using a D2Q9 lattice and BGK collision model for the three nonequilibrium computation variants NELI, SELI, and CELI (see Sec. III A and Table II). In this case, all the considered methods (ELIs and ZY methods) seem to lead to similar E_{rms} , with slightly less than second-order convergence. Only in the case of the “S” nonequilibrium treatment, the two parametrized linear methods, $K_2^- - \text{SELI} - \text{UL}$ and $K_2^- - \text{SELI} - \text{ULT}$, seem to be more accurate than the other schemes roughly by a factor of two. Nonetheless, that the fact that some variants are slightly better than the others or than existing methods like BFL and ZY, is very sensitive to the relaxation times, and the collision model. In fact, running the same experiment with TRT we observed similar slopes, but the relative accuracy of the methods may change. This aspect will be deepened in the following paragraphs.

b. Viscosity dependence. We verify the effectiveness of the parametrization on the E_{rms} in Fig. 7 for cylinder ratio $\beta = 0.2$. As expected, the error of the parametrized methods (either with K_1^- or K_2^-) is independent of the symmetric relaxation time (τ^+), provided that Λ is fixed (here $\Lambda = 1/8$ for which the bounce-back is exact in Poiseuille flow for general forcing treatment [13]). Both parametrization factors (K_1^- or K_2^-) provide a viscosity-independent behavior with a slight difference in accuracy for this steady-state condition. In general, all methods parametrized with K_1^- are equivalent at steady state, while the ones parametrized with K_2^- show different accuracies. The precision of the former group is identical (or extremely similar) to the one of the CLI/MGLI method [20]. This is expected given that the parametrization procedure of the CLI/MGLI is analogous to that of the K_1^- group.

The most accurate methods in this experiment are the fragmented nonparametric NELI-FL and NELI-FQ variants. Also, NELI-UL showed higher accuracy than BFL in the whole τ^+ range. Poor performances were instead detected for the nonparametric XELI-ULT (with X equal to N, S, or C). It is also remarkable that the nonparametric CELI-FL show perfectly overlapping results with BFL in Fig. 7 on the most at the left graph. Broadly speaking, the N and C nonequilibrium treatments lead to more exact and stable results. For the C version, the K_1^- and the K_2^- parametrizations are equivalent. We remind that the computation of K^- imposing two conditions. The first is that $\gamma^- \neq f(\Lambda^+)$. The second is either the LI/MGLI condition [20] (such that $\gamma^- = \Lambda\alpha^-$) for K_1^- or we ask that K^- does not depend upon the collision model for K_2^- . For the details please see Appendix D 3.

We recall here, that the CELI-UQ is automatically parametrized without any correction factor in accordance with Table II. Its viscosity-independence is confirmed in the most on the right graph of Fig. 7. Another remark is that despite the nonparametrized versions may show more accurate results than the parametrized ones in some intervals of $\tau^+ \propto \nu$, the *viscosity independence* property is important for all application where the apparent position of the boundary does not depend on the viscosity, e.g., in the computation of permeability through porous media.

c. Stability. Not all ELI schemes display the same stability properties. Figure 7 also contains a table that shows when instabilities have been detected. In the specific context of the TRT collision model with $\Lambda = 1/8$, the nonparametrized quadratic methods appear to be unstable for some values of τ^+ . In particular, the SELI-UQ and SELI-FQ are unstable in the large τ^+ region for mostly all possible values of τ^+ . Overall, XELI-YL and $K^- - \text{XELI} - \text{YL}$ ($X \in \{N, S, C\}$, $Y \in \{F, U\}$) schemes are the most stable; no instabilities have been detected for any τ^+ , neither in this benchmark nor in the impulsively started Couette flow treated afterward. Finally, XELI-YQ and $K^- - \text{XELI} - \text{YQ}$ ($X \in \{N, C\}$, $Y \in \{F, U\}$) are

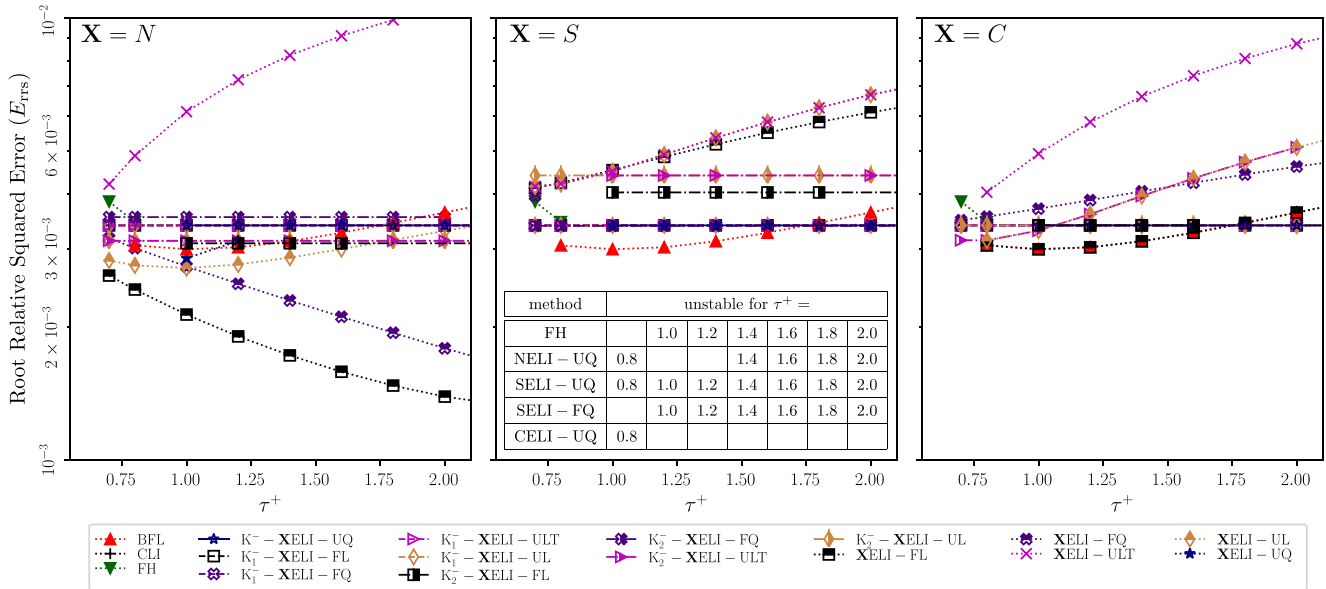


FIG. 7. E_{trs} error at steady state of ELI variants, BFL, CLI, and FH methods for increasing values of the symmetric relaxation time τ^+ . The simulations for which instabilities have been detected are listed in the table in the central figure (NB detected instabilities are relative to nonparametrized methods only). Results obtained using a D2Q9 lattice, TRT collision model ($\Lambda = 1/8$) and linear equilibrium.

the most delicate from the stability standpoint, but anyway stable for $\tau^+ > 1$.

d. Mass conservation. A common issue caused by interpolations is the violation of mass conservation. We investigated this concern computing the average density fluctuation $|\sum_i^N \frac{\rho_i/\rho_0}{N} - 1|$ (ρ_0 is the reference density) in the Taylor-Couette region at nondimensional time $t^* = t/t_{\text{ref}} = 5.0$, where $t_{\text{ref}} = (r_2 - r_1)/u$ and N is the number of nodes in the Taylor-Couette region; the results are presented in Fig. 8. Looking at the figure, the density fluctuation converges with a slope of the third or higher order.

Not all NELI schemes show the same mass conservation compliance. The most accurate NELI variant for mass conservation is the (K^-) -NELI-UQ. For this reason, the NELI-UQ is a particularly interesting method in the under-relaxed regime, commonly used for low Reynolds flows. Also, it worth mentioning that similar results can be obtained for the other XELI variants adopting different nonequilibrium treatments (SELI or CELI).

That being said, all enhanced-accuracy boundary rules, like the linear and parabolic MR, but also high-order accurate in-node variants like the LSOB, do not conserve the mass in the sense of the bounce-back rule. This means that the initial “mass” (sum of populations) is not necessarily preserved on the transient solutions. One could think at this point to implement a local artificial adjustment of mass, unfortunately, this has been shown to spoil the overall accuracy [77,78]. Moreover, the sum of the outgoing populations is not conserved locally on the exact modeling of parabolic grid-rotated profiles [10,19], where, however, the exact steady-state solution conserves the established global mass and the immobile populations reach their equilibrium. Otherwise, when an interpolation rule does not conserve the global outgoing mass, the post-collision solution of the immobile population uniformly recompensates

the established permanent mass leakage (there is a specific example for LI schemes in the recent work of Ref. [13] following Ref. [8]). In any case, we expect that the mass leakage does not spoil the accuracy of the established steady-state profiles because ρ plays here the role of a passive scalar.

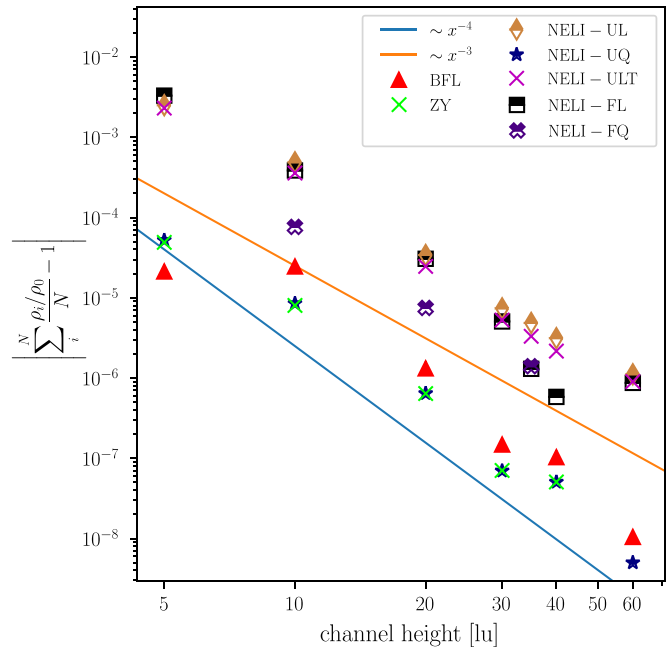


FIG. 8. Average density fluctuation, at dimensionless time $t^* = 5$ after the impulsive motion of the internal cylinder, as a function of the channel height in lattice units under diffusive scaling using a D2Q9 lattice, TRT collision model ($\Lambda = 1/8$, $\tau^+ = 2$) and linear equilibrium ($\text{Re} \ll 1$).

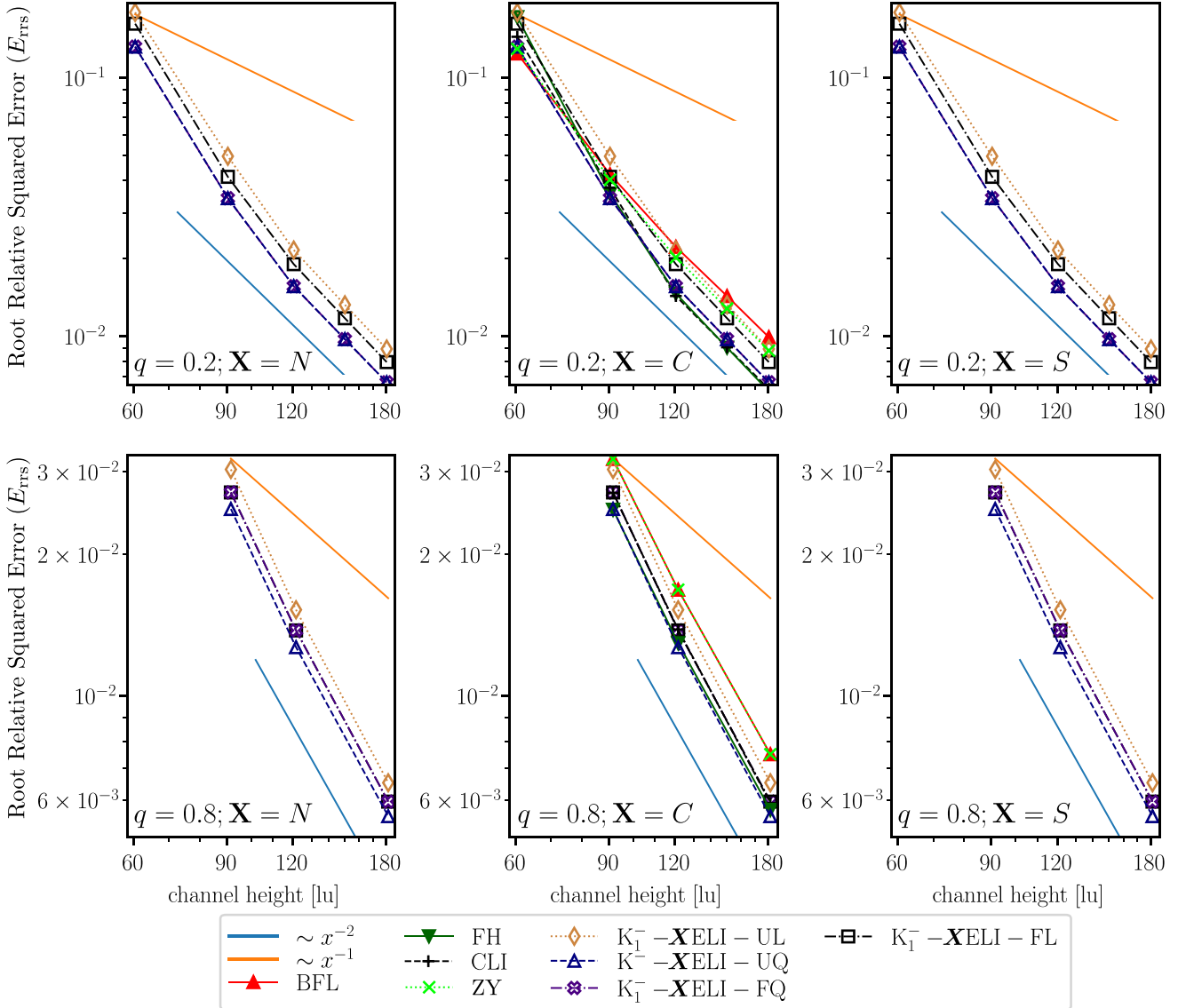


FIG. 9. Space convergence of E_{rms} at time is $t^* = 0.001$ of ELI variants, and for BFL, FH, CLI, ZY (in the central figures). The simulation was carried using a D2Q9 lattice, a TRT collision model ($\Lambda = 1/8$) and $Re = 1$.

To conclude, we think this aspect deserves to be investigated in future work, especially concerning the effective mass definition inside of shaped-boundary domains.

B. Impulsively started unsteady Couette flow

1. Description of the test case

The impulsively started Couette flow the fluid configuration is obtained abruptly moving one of the two parallel walls containing a quiet fluid, from the rest position to the constant velocity U . In this specific case, we consider the upper wall moving along the x direction and located at $y = h$ and the bottom one resting at $y = 0$.

In the context of low Reynolds number flows, convective phenomena can be neglected in the Navier-Stokes equation. Considering also the geometrical symmetries of the configuration, we can write the evolution equation of the

configuration [79]

$$\frac{\partial u}{\partial t} = \nu \frac{\partial^2 u}{\partial y^2}, \quad (41)$$

together with the following boundary and initial conditions:

$$\begin{aligned} u(0, t) &= 0, & \text{for all } t, \\ u(h, t) &= U, & \text{for } t > 0, \\ u(y, 0) &= 0, & \text{for } 0 \leq y < h. \end{aligned} \quad (42)$$

The problem defined by Eqs. (41) and (42) has a solution in the form of slow converging series [79]

$$u_{th}^* = \frac{u_{th}}{U} = \frac{y}{h} + \frac{2}{\pi} \sum_{n=1}^{\infty} \frac{(-1)^n}{n} e^{-n^2 \pi^2 \nu t / h^2} \sin \frac{n\pi y}{h}. \quad (43)$$

In Ref. [79] Erdoğan mentioned that at time $t^* = \nu t / h^2$ Eq. (43) truncated at the 54th term is sufficient to obtain a numerical solution compatible with a double floating point precision

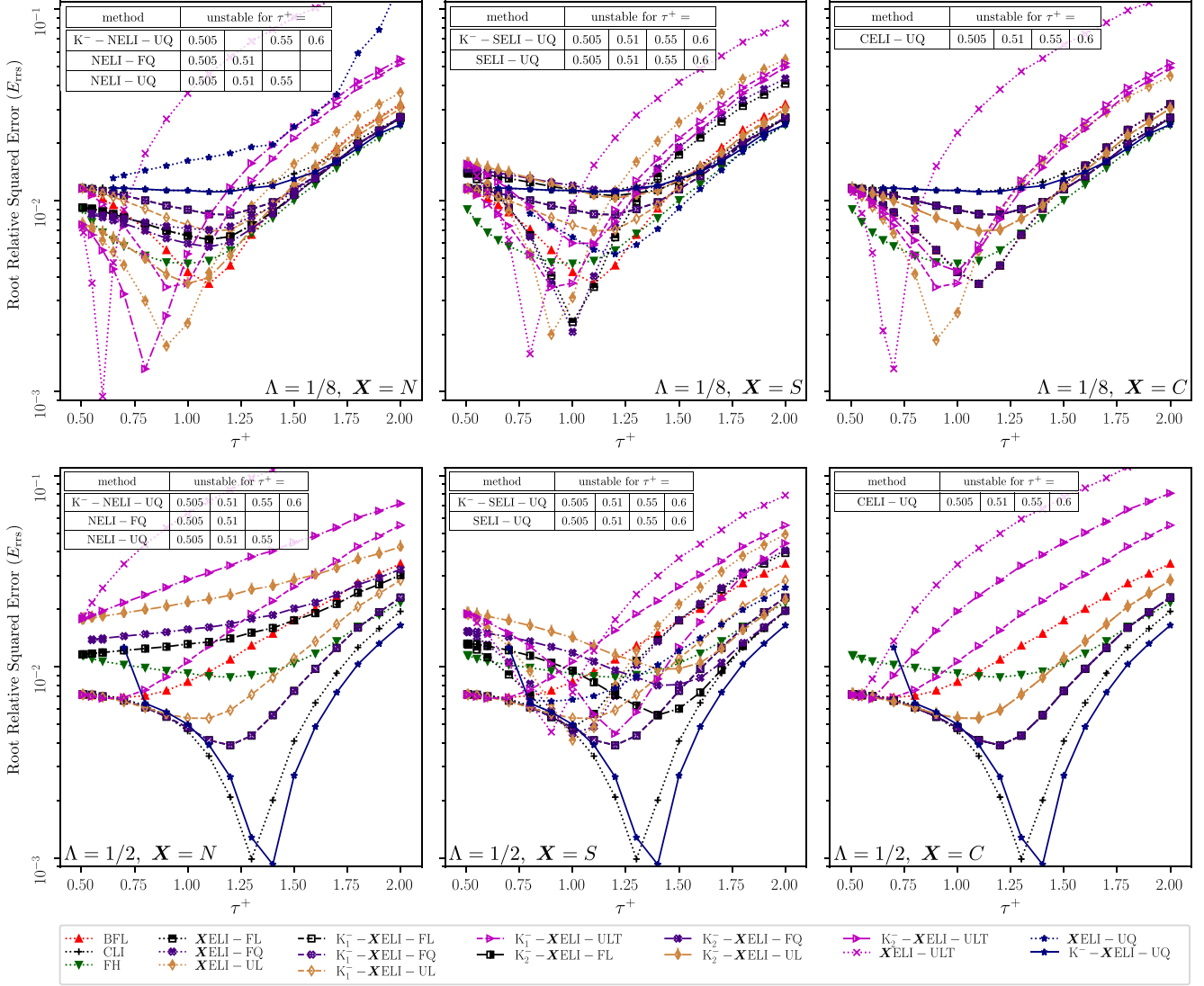


FIG. 10. Comparison of the error of the ELI method variants for different nonequilibrium component treatment (N,S,C), BFL, FH, and CLI, for two values of the magic parameter Λ as a function of the symmetric relaxation time τ^+ . Simulations characterized by channel height of $h = 91.6 \mu$ ($q = 0.8$) and $Re = 1$.

numerical simulation (given the computationally light evaluation, we used 100 terms).

We used the ELI variants, FH, CLI, and BFL to simulate the impulsively started Couette flow. The numerical domain is squared, bounded in the y direction by the walls, and by the periodic condition in the x direction. The LBM simulation is carried out with the D2Q9 lattice and either TRT or BGK collision model. The simulations are symmetric in the two dimensions and the top and bottom layer of nodes are located at $y = q$ and $y = h - q$.

The *root relative squared error* E_{rms} (also known as l^2 -norm error function), defined by Eq. (39) is used to evaluate the convergence of computational error, where u_{th}^* in this case is the theoretical dimensionless velocity norm given by Eq. (43).

2. Analysis of the results

We performed different experiments to verify the sensitivity of the accuracy (measured through the E_{rms}) to different

parameters. Herein, we will focus on low Reynolds number flows ($Re = 1$) using the TRT collision model. The accuracy will be evaluated at a snapshot of the flow at dimensionless time $t^* = 0.001$.

Going into more details, in Fig. 9 we verify that all the nonequilibrium variants of ELI (NELI, SELI, and CELI) show a second-order accuracy slope when the grid is refined under the *diffusive scaling* hypothesis. In the regime considered in Fig. 9, the accuracy shows low sensitivity to the chosen ELI nonequilibrium variant. In the same figure the results for BFL and ZY methods are presented, allowing us to infer that, under the considered conditions, the ELI, CLI, and FH methods are slightly more accurate than the former group.

In Figs. 10 and 11 we analyze the sensitivity of the error (E_{rms}) to the value of the viscosity relaxation time (τ^+), keeping the parameter Λ constant. In particular, Fig. 10 presents an extensive comparison of all variants for two different values of the magic parameter Λ in the case of $q = 0.9$. On the contrary, Fig. 11 shows the comparison for a selected

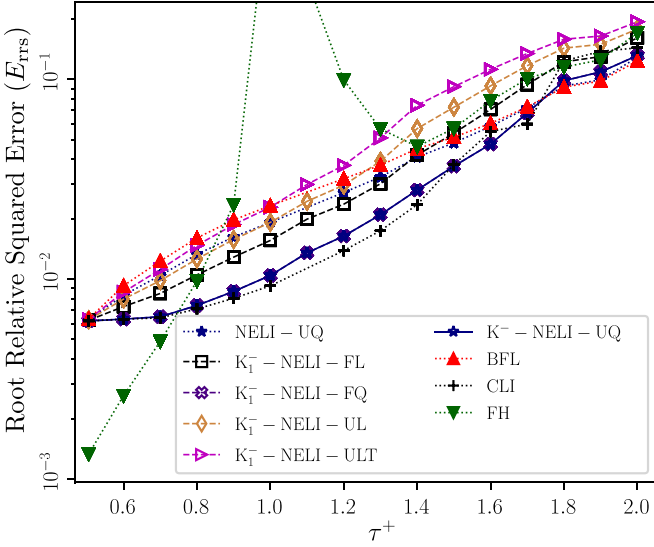


FIG. 11. Sensitivity of the E_{rms} error to symmetric relaxation time τ^+ , in the case of impulsively started Couette flow. The experiment refers to a dimensionless time of $t^* = 0.001$ for $q = 0.2$ and $Re = 1$. The simulation was carried using a D2Q9 lattice with 60 nodes in the vertical direction and a TRT collision model ($\Lambda = 1/8$). Results for BFL, CLI, and FH are shown for comparison.

number of variants (the NELI and K_1^- -NELI) for $q = 0.2$. Considering Fig. 10, one can see that the magic parameter Λ of the TRT, influences the relative accuracy of different methods. Some methods are, in fact, advantageous in some particular range of parameters. In particular, the ELI-UL and the ELI-ULT presents a low error (E_{rms}) when $\Lambda = 1/8$ in the over-relaxed regime ($\tau^+ < 1$). On the contrary, the ELI-UQ shows good accuracy when $\Lambda = 1/2$ in the under-relaxed operation regime ($\tau^+ > 1$). In this range, its accuracy is the same as for CLI. This is in agreement with the numerical analysis, given that both CLI and ELI-UQ have the same underlying steady-state closure relation (they both operate with $a_2 = 1$). The difference in accuracy for $\tau^+ \rightarrow 1/2$ between the two methods could be therefore related to the different time-dependent approximation. In Fig. 11 ($q = 0.2$) the error increases monotonically with τ^+ as a consequence of the loss in the time resolution. For $q = 0.2$ along the whole spectrum of values considered for τ^+ , the NELI variants show a lower E_{rms} than BFL. Notably, while the parametrized ELI methods with K_1 , BFL, ZY, and CLI converge toward the same solution for $\tau^+ \rightarrow 1/2$, the FH method shows a very good accuracy in this limit, despite the known regime of instability for intermediate values of τ^+ . One can additionally notice that the ELI-FQ and ELI-UQ show similar or equal behavior of the CLI method [20].

Figure 12 investigates the impact of the different parametrization constants K_1^- and K_2^- proposed in Sec. V A (Table II) on the error of the NELI variant. The K_1^- and K_2^- constants results in similar errors in the under-relaxation regime ($\tau^+ > 1$). On the contrary, in the over-relaxation regime choosing K_1^- leads to more accurate results. This suggests that users interested purely in the under-relaxation regime can benefit from the easier expression of the K_2^- constant, without appreciable loss of accuracy. We recall here

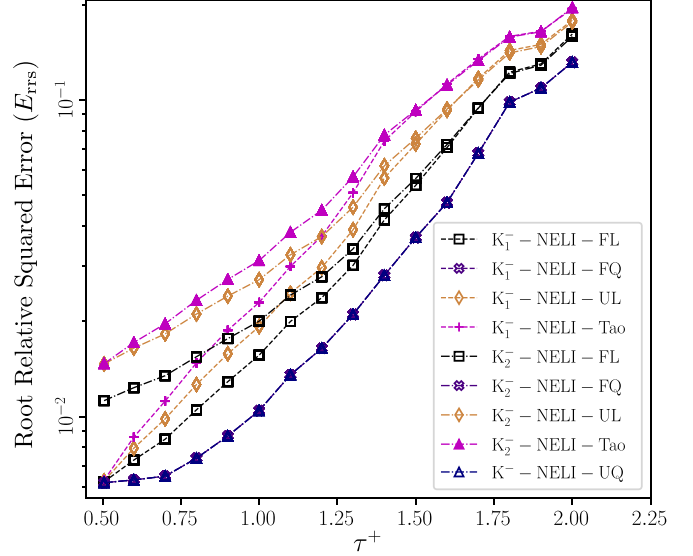


FIG. 12. Comparison of accuracy at transient state for different parametrization of the boundary scheme (K_1^- or K_2^-), in the case of impulsively started Couette flow. The experiment is referred to a dimensionless time of $t^* = 0.001$ for $q = 0.2$ and $Re = 1$. The simulation was carried using a D2Q9 lattice and a TRT collision model ($\Lambda = 1/8$).

that for the ELI-UQ $K_1^- = K_2^- = K^-$, therefore a unique line is shown for it in Fig. 12. Figure 14, described afterward, confirms that also for the CELI variant at $\tau^+ = 2$ the results for K_1^- and K_2^- are overlapping (except for the CELI-ULT method for which the choice of K_2^- results in a loss of accuracy).

The effect of changing the normalized distance of the wall from the first line of nodes q can be appreciated by looking at Fig. 13. As predicted by the theory, BFL and all ELI variants, but the NELI-UL reduce to the HW for $q = 1/2$. One may also

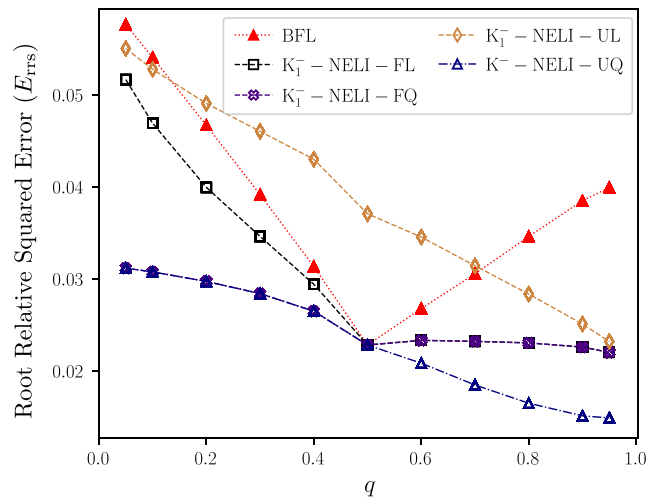


FIG. 13. Sensitivity of the E_{rms} error to normalized distance from the wall q . The experiment refers to a dimensionless time of $t^* = 0.001$. The results of BFL are shown for comparison. The simulation was carried using a D2Q9 lattice with 60 nodes in the vertical direction and a TRT collision model ($\Lambda = 1/2$, $\tau^+ = 2$).

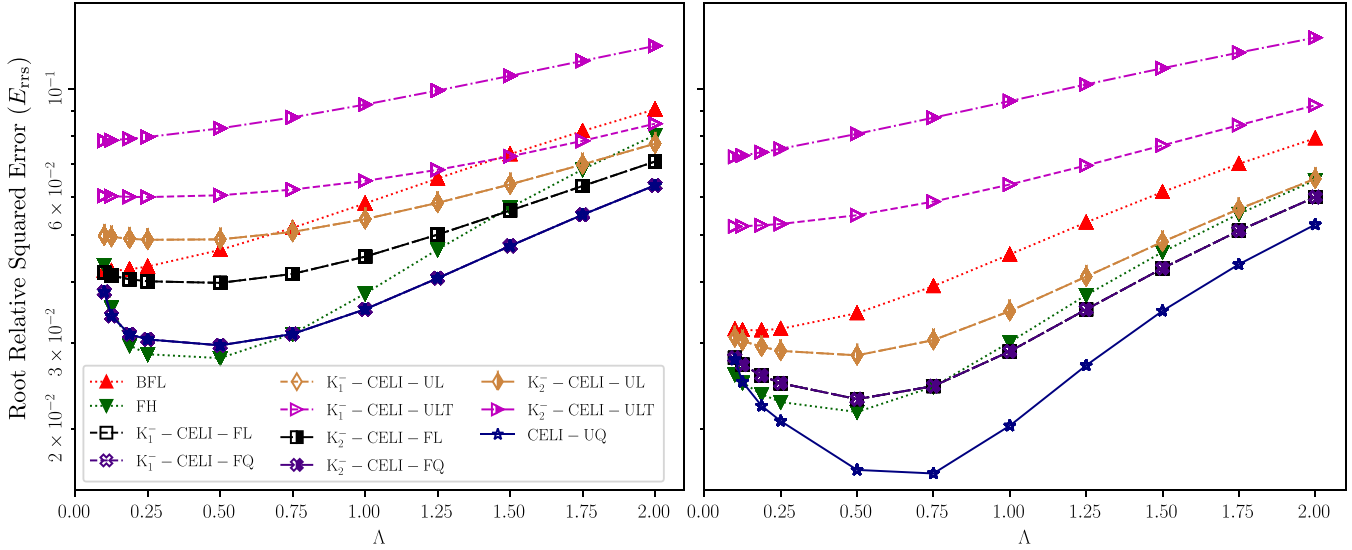


FIG. 14. Sensitivity of the E_{rrs} error to the magic parameter Λ , in the case of impulsively started Couette flow, for CELI, BFL, and FH. The experiment is referred to a dimensionless time of $t^* = 0.001$. *Left*: $q = 0.2$; *Right*: $q = 0.8$.

notice that for $q < 1/2$, NELI-FQ and NELI-UQ show overlapping results. *Vice versa*, for $q > 1/2$ one can see overlapping results for NELI-FQ and NELI-FL.

We computed the E_{rrs} for increasing values of Λ at constant $\tau^+ = 2$, for $q = 0.2$ and $q = 0.8$, in Fig. 14. For both the values of q , the CELI variants show better accuracy than the BFL method. Interestingly, while BFL seems to have the best accuracy for Λ approaching zero, the CELI variants and the FH seem to have an optimal accuracy for $\Lambda \in [1/4, 3/4]$, which is typically more stable interval.

Finally, the evolution of E_{rrs} in the (τ^+, Λ) space is evaluated in Fig. 15. The surfaces in the figure have been built from multiple simulations, one for each line intersection visible on the surfaces. In general, the error increases with τ^+ and Λ , but this is not always true for all methods and in all conditions. The shapes of the surfaces associated with different methods are different and nonlinear, suggesting that in the TRT context, talking about the accuracy of a method makes sense for a defined combination of τ^+ and Λ , in agreement with the expectations from the transient truncation and stability analysis.

C. Jeffery’s orbit: Ellipsoidal cylinder and ellipsoid rotation

With this test case, we want to evaluate the capability of the NELI variants to properly simulate a rigid solid body immersed in viscous fluid flow. In particular, we couple the boundary condition with a technique to suppress numerical noise associated with the motion of the boundary across the fluid lattice nodes [80]. This section will be more focused on the *qualitative* observation of the results, rather than on precise estimation of the numerical errors. The aim is to give evidence of the suitability of the proposed schemes for fluid-solid interaction.

1. Description of the test case

Jeffery’s orbit is a common benchmark test for curved boundary conditions. It describes the rotation of ellipsoidal objects induced by a shear flow in Stoke’s regime [81]. There-

fore, it is well suited to verify the capability of a numerical method to describe a fluid-solid interaction problem. In our experiment, the ellipsoid is located at the center of a channel. The channel is delimited in the y direction by two horizontal walls, among which the upper is impulsively started to move along the x direction at the beginning of the simulation with the fluid at rest. In the initial condition, the prolate ellipsoid

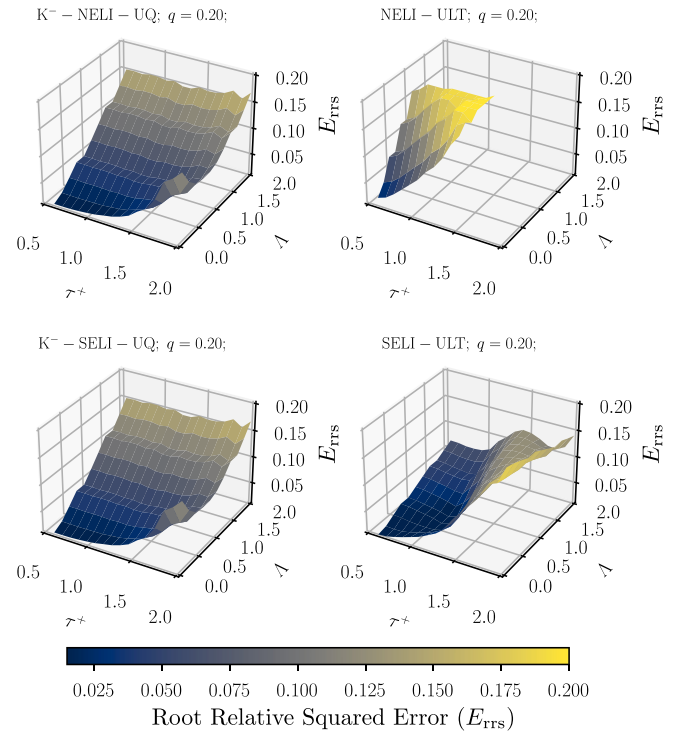


FIG. 15. E_{rrs} error as a function of the symmetric relaxation time τ^+ and of the TRT magic parameter Λ . Each mesh vertex corresponds to a different simulation at $t^* = 0.001$ and channel height $h = 60.4$ lu.

lies at the center of the channel, in a vertical position, with its longer diameter aligned with the y direction. The computational domain is periodic in the x and z directions. At the time $t = 0$ the upper wall is abruptly accelerated to its terminal velocity u_{lid} , such that it generates the following strain rate in the channel

$$\dot{\gamma} = \frac{u_{\text{lid}}}{H}, \quad (44)$$

where H is the channel height. The ellipsoid start accelerating until it reaches its steady-state Jeffery's orbit, that reads [81]

$$\dot{\theta} = \frac{\dot{\gamma}}{r_e^2 + 1} (r_e^2 \cos^2 \theta + \sin^2 \theta), \quad (45)$$

where θ is the inclination of the ellipsoid axis corresponding to the major radius r_a with respect to the y axis (the vertical one), $\dot{\theta}$ is the corresponding angular velocity, and $r_e = \sqrt{r_a^2 + 2 \cdot r_b^2}$ is the equivalent radius. The Reynolds number in this scenario is redefined with the shear stress

$$\text{Re} = \frac{\dot{\gamma} r_e^2}{\nu} = \frac{u_{\text{lid}} r_e^2 / H}{\nu}. \quad (46)$$

In this experiment, we describe the ellipsoid with a thin-shell surface whose dynamics are computed following the rigid body motion equations. The thin-shell representing the ellipsoid is filled with fluid. Nevertheless, the internal fluid is virtual and has ideally no impact on the dynamics. This because the forces from the fluid to the rigid body are computed only considering the external fluid, using Eq. (E1) in Appendix E 1.

2. Analysis of the results

All the investigated methods (nonparametric NELI variants) lead to similar values of the ellipsoid angular velocity evolution in time in the case of a prolate ellipsoid with a diameter ratio $\beta = r_a/r_b = 2$. In particular, in Fig. 16, we compared the results of a 3D ellipsoid angular velocity evolution for the HW, BFL, and the present NELI-FQ, but the results are similar for all the nonparametric NELI variants.

a. Numerical noise. When dealing with moving boundaries, LBM boundary methods give rise to spurious pressure oscillations. One of the principal sources of these oscillations is the results of some nodes, named *fresh nodes*, changing the side of the boundary surface. In the upwind part of the surface *fresh nodes* appear as uninitialized nodes with wrong populations' values: this causes the triggering of pressure waves. The process of recomputing the values for the distribution functions in the *fresh nodes* is called *refilling* and can reduce the magnitude of pressure oscillations. The *refilling* is an active research topic [45,80,82]. In particular, in the recent extensive comparison [80], the authors indicate the *local iteration refilling* (LIR) [45] as the most effective in reducing oscillations. For this reason, we choose LIR to correct the spurious pressure oscillations, implementing it in a slightly modified version (see Appendix E 3). In our experiments, using a thin-shell approach, the simulations are stable even if no refilling algorithm is used. Therefore, we tested different boundary conditions before and after the LIR implementation.

The pressure oscillations due to the boundary motion are transferred to the rigid body through the momentum coupling,

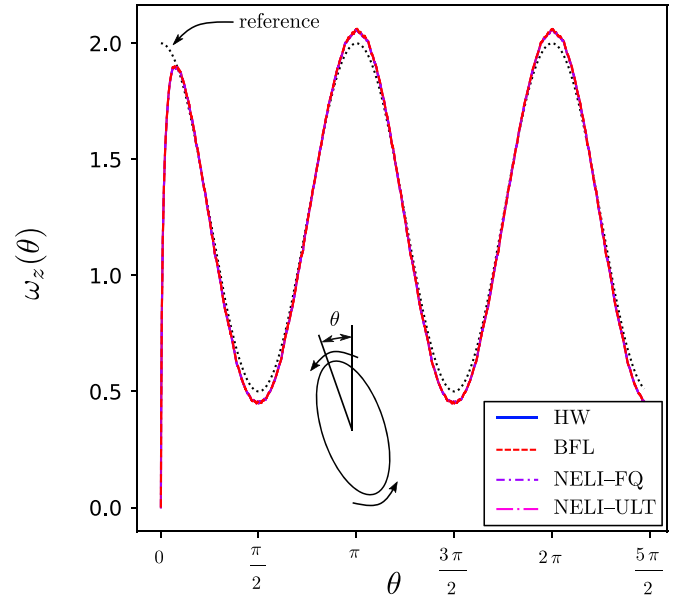


FIG. 16. Angular velocity of the Jeffery's orbit described by a 3D prolate ellipsoid characterized by a ratio of radii $\beta = r_a/r_b = 2$. The solutions of HW, BFL, NELI-FQ, and NELI-ULT schemes (nonparametric) are compared with the analytical solution (black dashed line). Parameters of the simulations: $\tau = 2$, BGK collision model, $\text{Re} = 4$, $H = 10r_e$ (channel height), $r_e = \sqrt{r_a^2 + 2 \cdot r_b^2} = 30$ (equivalent radius).

leading to a noisy torque time evolution. The measure of the oscillations in the torque acting on the rigid body is a common way to estimate the magnitude of pressure oscillations [80,83,84]. It is anyhow important to notice that perturbations in the torque acting on the body are only an indirect measure of the effect of pressure waves and can be also influenced by the techniques used for the force computation.

We decided to use a qualitative approach to compute the torque squared fluctuation that allows producing smooth graphs that are easy to compare. The detail of the computations is shown in Appendix E 2. Here, we only point out that the presented values of the torque squared fluctuation are interpolated values using the best fitting polynomials. Therefore, they should be interpreted as *qualitative* measures that do not aim at accurate measurements.

Using the momentum exchange algorithm and without refilling techniques, local methods show higher fluctuations (Fig. 17). Nevertheless, after the LIR implementation both local and nonlocal interpolated methods show similar performance in terms of torque-squared fluctuation (Fig. 17). To summarize, the considered NELI variants show good stability property in the simulation of a fluid-rigid body problem interaction. The ELI leads to results comparable with BFL for the ellipsoid dynamics, both in terms of angular velocity evolution and in terms of torque fluctuation. Nevertheless, for the local methods, the refill algorithm appears to be important to reduce the effects on the torque due to the pressure oscillation, mainly because the *single-node* schemes increase the coupling between the first layer of nodes close to the surface and the rigid body motion.

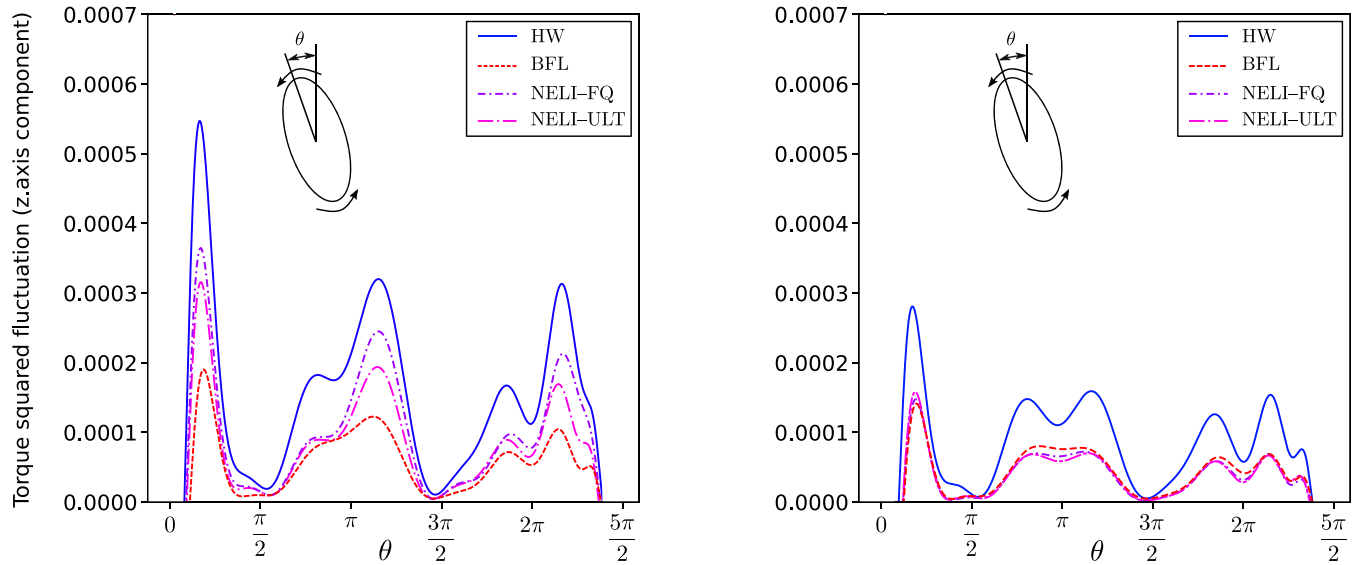


FIG. 17. Jeffery’s orbit described by a 3D prolate ellipsoid characterized by a ratio of radii $\lambda = r_a/r_b = 2$. Plots of the squared fluctuation of the torque obtained with Eq. (E4). (left) Without LIR refilling, (right) with LIR refilling.

VII. CONCLUSIONS

In this article, we presented a class of enhanced single-node boundary conditions (ELI). The *enhancement* theoretically derives from the introduction of wall populations and from the optimization interpolation and parametrization coefficients of the general ELI Eq. (13). The ELI method represents a family of an infinite number of schemes characterized by two free tunable coefficients and a parametrization constant K^- . The most physically meaningful members can be singled out using the proposed generalized methodology for the computation of the interpolation coefficients.

The resulting boundary methods are *single node*, which means that they are suitable to simulate narrow gaps, without introducing special conditions. This *physical locality* feature of the ELI facilitates the management of such singular shapes allowing a uniform implementation in the whole domain. Thus, ELI can be implemented either in an *algorithmically nonlocal* or *algorithmically local* way without any need of introducing particular cases in presence of narrow portions of space containing only one lattice node along a lattice direction. Moreover, in the case of a *algorithmically local* implementation, no data needs to be recovered from the neighboring cells in parallel simulations, improving conceivably the parallel computing performances. Therefore, ELI boundary conditions are expected to be attractive for GPU based implementations.

Several variants of the ELI scheme have been proposed in the present article. For each one, we provide an additional parametrization that leads to viscosity independent accuracy at the steady state. The combination of the *locality* of the schemes and *viscosity independent errors* at the steady state is particularly interesting for porous media applications. Indeed, both these characteristics are crucial for achieving easy to implement, accurate, and viscosity independent permeability estimations.

We verified that both the proposed parametrizations are effectively viscosity independent and accurate. From our

(time-dependent) results, the easier to implement parametrization (K_2^-) seems to provide overlapping results to the other one (K_1^-) in the under-relaxed operating regime (high viscosity). Moreover, the K_2^- parametrization is collision independent and extends straightforwardly to MRT collision models. On the other side, only the parametrization by K_1^- allows for equivalent solutions in pressure-gradient and force-driven flow. We stress that all our methods and results remain valid with the standard MRT collision models provided that their additional degrees of freedom are parametrized accordingly to work [11].

Out of the ELI variants, the XELI-UQ is automatically parametrized without any K^- correction using the “X = C” treatment for the wall nonequilibrium (i.e., the CELI-UQ). This scheme is accurate, easy to implement, and stable in the under-relaxed range. In this span, it shows similar or equal accuracy of CLI [8], both for the steady- and time-dependent case. The theoretical analysis of their steady-state closure relations confirms that XELI schemes have the formal linear accuracy of LI, and the parametrized XELIs have the one of MGLI. As a consequence, the different stability characteristic in the time-dependent over-relaxed range is probably related to the different time-dependent approximation. Finally, CELI-UQ exhibits a small mass conservation violation, comparable or smaller than the one of the BFL. However, we note that mass conservation and accuracy are not equivalent. For example, HW is mass-conserving but inaccurate on shaped walls.

Among the nonparametrized ELI variants, the NELI-FL and the CELI-FL showed an interesting behavior. Considering the steady-state cylindrical Couette-flow, the first showed better than average accuracy for the velocity field; the latter results in the same precision as the BFL method.

We also showed that the method recently proposed by Tao *et al.* [17] (NELI-ULT) can be interpreted as a variant of the ELI family. As for the other variants, we provided a parametrized version also for this scheme. The results for this method display low accuracy for high-viscosity, but good

results for low-viscosity (over-relaxation regime, $\tau^+ < 1$). Another similar variant is the XELI–UL that has the advantage to be more accurate for higher relaxation times. The main limitation of these linear unified schemes (UL) is that they suffer from higher mass conservation violations. This could be related to the fact that they do not come down to the half-way bounce-back when the boundaries are located in the middle of two lattice nodes. In our future work, we would like to better understand the correlation between the formal spatial and temporal accuracy, on the one hand, and the global mass conservation, on the other.

Performing the different time-dependent test cases with the TRT, we observed that generally, the relative accuracy of the various ELI schemes and other methods (like BFL, FH, and ZY) is strictly dependent on the combination of the TRT magic parameter and the symmetric relaxation time τ^+ . In other words, the temporal accuracy depends on two independent relaxation rates, in agreement with the truncation analysis. The same conclusion applies to stability. This evidence highlights how results obtained under specific conditions could easily lead to improper judgments on the considered scheme. We stress that wall-populations might be evaluated at noninteger time steps to fit the wall-advancing strategy. For this reason, the availability of many spatially equivalent schemes is advantageous because it will allow to further fine-tune ELI and LI schemes improving their time accuracy according to the time-dependent analysis of the underlying closure relations. In parallel, it will be interesting to conduct systematic studies to compare their actual stability. We emphasize that any combinations of similar ELI and LI schemes are possible. For example, CLI in the bulk with CELI-UQ in corners.

The novel class of boundary conditions is suitable to describe moving boundaries immersed in the fluid, specifically a rigid body in a shear flow. We verified NELI–FQ and NELI–ULT that proved to be stable and well-behaving. Besides, the *local iteration refill* algorithm [45] has proved to be a good companion for the ELI. After its adoption, single-node techniques and the BFL method showed the same noise level on the torque acting on the rigid body.

We plan to extend our boundary approach to weakly compressible parametrized TRT models [74] and for more compact parabolic-accurate schemes [85].

ACKNOWLEDGMENTS

Fruitful discussions with Orestis Malaspinas, Christophe Coreixas, and Christos Kotsalos are gratefully acknowledged. This project has received funding from the European Union’s Horizon 2020 research and innovation programme under Grant Agreement No. 823712 (CompBioMed2 project).

APPENDIX A: ADDITIONAL AND COMPLEMENTARY FORMULAS

1. Redefinition of population for the trapezoidal integration

The populations expressed in lattice units and denoted with the symbol f can be redefined using the trapezoidal integration

and denoted by the symbol f . Their expression reads:

$$f_i(\mathbf{x}, t) = f_i(\mathbf{x}, t) + \frac{1}{2\bar{\tau}} f_i^{\text{neq}}, \quad (\text{A1})$$

$$f_i^{\text{neq}} = f_i(\mathbf{x}, t) - f_i^{\text{eq}}(\mathbf{x}, t), \quad (\text{A2})$$

$$f_i^{\text{eq}} = f_i^{\text{eq}}, \quad (\text{A3})$$

$$\tau = \bar{\tau} + 1/2. \quad (\text{A4})$$

2. ELI method in generalized coordinate s

Rewriting the ELI formula in terms of the generalized coordinate s can be particularly interesting to simplify implementation. In fact, the coordinate $s = s(t + 1)$ represents the signed distance from the wall of the interpolating populations at time step $t + 1$. For example, the population $f(1 - q)$ was located at $s(t) = -q$ (i.e., \mathbf{x}_F) at time t and it is located at $s = 1 - q$ at $t + 1$, that means \mathbf{x}_B after applying the usual streaming step. The ELI Eq. (13) in s coordinates reads

$$\begin{aligned} f(q) = & a_1 f(-q) + \\ & + a_2 \left(\underbrace{f(1-q) + 2f^{\text{eq}-}}_{\text{HW [6, 7]}} \right) + \\ & + a_3 f(1+q) + a_4 \underbrace{f(0)}_{\text{by Tao et al. [17]}} + \\ & + a_5 \underbrace{f(1)}_{\text{new ELI}} - \underbrace{K^- \frac{f^{\text{neq}-}(1+q)}{\tau^-}}_{\text{optional sec. IV B}} \end{aligned} \quad (\text{A5})$$

APPENDIX B: DIFFUSIVE SCALING AND LATTICE UNITS

1. Diffusive scaling

In the *quasi*-incompressible LBM, the reference system of the lattice has peculiar properties. Consider the dimensionless form of the Boltzmann Eq. (1):

$$\text{Ma} \partial_t f^* + \partial_\alpha \xi_\alpha^* f^* = \frac{1}{\text{Kn}} \mathcal{Q}_{\text{BE}}^*. \quad (\text{B1})$$

In canonical reference frames, the dimensionless numbers Ma and Kn are invariant with respect to the change of units system. In other terms, they are the physical *degrees of freedom* that determines the dynamic properties of the system. The Boltzmann equation, written in different units having the same dimensionless numbers Ma and Kn (and also Re via the Von Karman relation), describes systems with the same dynamic properties, thanks to Eq. (B1). We can say that the system “scales” with Kn and Ma as fixed points, moving from one reference to the other:

$$\text{Ma} = \text{Ma}_1 = \text{Ma}_2, \quad \text{Kn} = \text{Kn}_1 = \text{Kn}_2, \quad (\text{B2})$$

where the indexes refer to the reference systems. This type of scaling preserves the dynamical properties of the system, moving from one reference to the other. Unfortunately, choosing this type of physical scaling does not allow to keep the speed of sound c_s constant in lattice units. In fact, the relation Eq. (B2), requires that the speed of sound and the mean free path stay constant in nondimensional units during the scaling.

An alternative scaling, is the *diffusive scaling*. In this case we assume that the dimensionless grid spacing δx^* and the mean-free-path ℓ^* are proportional, i.e., $\delta x^* \propto \ell^*$ and that the speed of sound is invariant in lattice units. Mathematically speaking, the *diffusive scaling* conditions reads:

$$\text{Re} = \text{Re}_1 = \text{Re}_2, \quad \text{Kn} = \text{Ma}_1 = \text{Ma}_2 \neq \text{Kn}_1 \neq \text{Kn}_2. \quad (\text{B3})$$

Equation (B3) says that the description of the same system from the point of view of two different lattices will result in different compressible descriptions (different Kn) but in identical incompressible descriptions thanks to $\text{Re}_1 = \text{Re}_2$. A direct consequence of Eq. (B3) is that

$$\delta x^{*2} = \delta t^*. \quad (\text{B4})$$

2. Lattice units

The *lattice units* are a unit system for the lattice reference frame. As a consequence, equations written in lattice units inherit the assumptions made for the lattice scaling (e.g. the diffusive scaling). Using Eq. (B4), it is possible to recover the following relevant relation:

$$\frac{\partial}{\partial t} = \text{Kn} \frac{\partial}{\partial x}, \quad (\text{B5})$$

where the variables x and t are in lattice units. Equation (B5) is important in the scale separation during the Chapman-Enskog expansion (Appendix C).

APPENDIX C: CHAPMAN-ENSKOG EXPANSION OF TRT-LBE

The Chapman-Enskog expansion [49] is a *lifting* procedure [86] that aims to correlate the macroscopic hydrodynamics fields to a reduced-order distribution function f_c that is completely determined by them and sufficient to describe their dynamics properties at the Navier-Stokes level. In other terms, the continuum full-order kinetic distribution function f and the reduced order one f_c are constrained to produce the same observable at the macroscopic level. The Chapman-Enskog expansion makes the additional *ansatz* that the reduced distribution f_c depends upon time only *via* the collisional invariant moments m_0 , m_1 , and m_2 ,

$$f_c = f_c(\xi, m_0(\mathbf{x}, t), m_1(\mathbf{x}, t), m_2(\mathbf{x}, t), \mathcal{X}), \quad (\text{C1})$$

$$\partial_t f_c = \partial_{m_0} f_c \partial_t m_0 + \partial_{m_1} f_c \partial_t m_1 + \partial_{m_2} f_c \partial_t m_2. \quad (\text{C2})$$

The reduced-order distribution function f_c is then expanded in terms which magnitudes are proportional to the various power

of the Knudsen number, that in this context we identify with the letter ϵ to be compliant with the classical notation ($\epsilon = \text{Kn}$)

$$f_c = \sum_{n=0}^{\infty} \epsilon^n f_c^{(n)}. \quad (\text{C3})$$

In a similar fashion, also the partial derivatives are expanded

$$\partial_\alpha = \sum_{n=1}^{\infty} \epsilon^n \partial_\alpha^{(n)} \quad \partial_t = \sum_{n=1}^{\infty} \epsilon^n \partial_t^{(n)}, \quad (\text{C4})$$

where the operators that constitute the partial derivatives are defined depending on how they act on the macroscopic moments. In the case of the Navier-Stokes hydrodynamic regimes, the expansion reads

$$\begin{aligned} f_c &= f_c^{\text{eq}} + \epsilon f_c^{(1)} + \epsilon^2 f_c^{(2)} = f_c^{\text{eq}} + f_c^{\text{neq}}, \\ \partial_t &= \epsilon \partial_t^{(1)} + \epsilon^2 \partial_t^{(2)} \quad \partial_\alpha = \epsilon \partial_\alpha^{(1)}, \end{aligned} \quad (\text{C5})$$

where $f_c^{\text{eq}} = f_c^{(0)}$. For the LBM populations, the previous expansion can be expressed in lattice units under *diffusive scaling* hypothesis, using Eq. (B5):

$$\begin{aligned} f_{c,i} &= f_{c,i}^{\text{eq}} + \epsilon f_{c,i}^{(1)} + \epsilon^2 f_{c,i}^{(2)} = f_{c,i}^{\text{eq}} + f_{c,i}^{\text{neq}}, \\ \partial_t &= \epsilon^2 \partial_t^{(2)}, \quad \partial_\alpha = \epsilon \partial_\alpha^{(1)}. \end{aligned} \quad (\text{C6})$$

Equations (C6) are then substituted in the Taylor expansion of the TRT-LBE Eq. (7a) [20,70],

$$f_{c,i}^\pm + (\partial_t + c_{i\alpha} \partial_\alpha) f_{c,i}^\pm + (\partial_t + c_{i\alpha} \partial_\alpha)^2 \frac{f_{c,i}^\pm}{2} = f_{c,i}^\pm - \frac{f_{c,i}^{\text{neq}\pm}}{\tau^\pm}, \quad (\text{C7})$$

leading to

$$\begin{aligned} &(\epsilon \partial_t^{(1)} + \epsilon c_{i\alpha} \partial_\alpha^{(1)} + \epsilon^2 \partial_t^{(2)}) (f_{c,i}^{\text{eq}\pm} + \epsilon f_{c,i}^{(1)\pm}) \\ &+ (\epsilon \partial_t^{(1)} + \epsilon c_{i\alpha} \partial_\alpha^{(1)})^2 \frac{(f_{c,i}^{\text{eq}\pm} + \epsilon f_{c,i}^{(1)\pm})}{2} + \mathcal{O}(\epsilon^3) \\ &= -\frac{\epsilon f_{c,i}^{(1)\pm} + \epsilon^2 f_{c,i}^{(2)\pm}}{\tau^\pm}, \end{aligned} \quad (\text{C8})$$

where, terms with Knudsen order higher than two, have been omitted. Rearranging the previous equation and separating the terms associated with ϵ^1 and ϵ^2 we get

$$\epsilon^1 : \frac{f_{c,i}^{\pm(1)}}{\tau^\pm} = -c_{i\alpha} \partial_\alpha^{(1)} f_{c,i}^{\text{eq}\mp}, \quad (\text{C9a})$$

$$\epsilon^2 : \frac{f_{c,i}^{\pm(2)}}{\tau^\pm} = -\partial_t^{(2)} f_{c,i}^{\text{eq}\pm} + (c_{i\alpha} \partial_\alpha^{(1)})^2 f_{c,i}^{\text{eq}\pm} \Lambda^\mp. \quad (\text{C9b})$$

APPENDIX D: CLOSURE RELATIONS AND PARAMETRIZATION

1. Details of the procedure

In this section, we report the explicit computations for each step (enumerated by the list) reported in Sec. IV B. We remark that we considered the values of the wall populations at integer times t and $t + 1$, however, this is not a compulsory choice, as stressed in Sec. III A. Therefore, the following analysis should not be considered exhaustive for the time-dependent terms.

Steps 1 and 2: In the following equation, the underlined term is zero for the CELI scheme. It is summed (+) for NELI and subtracted (−) for SELI. The canceled terms are set to zero because they are higher-order. The time-space location of the population has to be intended at time t and location \mathbf{x}_F when not otherwise indicated. For conciseness, we define the relaxation

rates $\omega^\pm = 1/\tau^\pm$, and use them in the following:

$$\begin{aligned}
f_i^{\text{eq}+} - f_i^{\text{eq}-} + f_i^{\text{neq}+} - f_i^{\text{neq}-} &= +a_2[f_i^{\text{eq}+} + f_i^{\text{eq}-} + (1 - \omega^+)f_i^{\text{neq}+} + (1 - \omega^-)f_i^{\text{neq}-}] - 2a_2f_i^{\text{eq}-}\Big|_{x_W}^t \\
&+ \partial_t f_i^{\text{eq}+} - \partial_t f_i^{\text{eq}-} + \partial_t f_i^{\text{neq}+} - \partial_t f_i^{\text{neq}-} + a_3[f_i^{\text{eq}+} - f_i^{\text{eq}-} + (1 - \omega^+)f_i^{\text{neq}+} - (1 - \omega^-)f_i^{\text{neq}-}] \\
&+ \frac{\partial_t^2}{2} f_i^{\text{eq}+} - \frac{\partial_t^2}{2} f_i^{\text{eq}-} + \frac{\partial_t^2}{2} f_i^{\text{neq}+} - \frac{\partial_t^2}{2} f_i^{\text{neq}-} + a_4[f_i^{\text{eq}+} - f_i^{\text{eq}-}]_{x_W}^{t+1} \\
&+ a_4[f_i^{\text{eq}+} - f_i^{\text{eq}-}]_{x_W}^{t+1} \\
&+ a_4[f_i^{\text{eq}+} - f_i^{\text{eq}-}]_{x_W}^{t+1} \\
&+ a_4[f_i^{\text{neq}+} + f_i^{\text{neq}-}]_{x_W}^{t+1} \\
&+ a_5[f_i^{\text{eq}+} - f_i^{\text{eq}-}]_{x_W}^t \\
&+ a_5[(1 - \omega^+)f_i^{\text{neq}+} \pm (1 - \omega^-)f_i^{\text{neq}-}]_{x_W}^t - K^- \frac{f_i^{\text{neq}-}(x_F)}{\tau^-}. \tag{D1}
\end{aligned}$$

Rearrangement: In the following equation, the underlined terms can be neglected under *diffusive scaling hypothesis* considering Eq. (C6):

$$\begin{aligned}
[f_i^{\text{eq}+}(-a_4 - a_5) + f_i^{\text{eq}-}(a_4 + a_5 + 2a_2)]_{x_W}^{t+1} &= f_i^{\text{eq}+}(a_2 + a_3 - 1) + f_i^{\text{eq}-}(a_2 - a_3 + 1) \\
&+ f_i^{\text{neq}+}(a_2(1 - \omega^+) + a_3(1 - \omega^+) + a_4 + a_5(1 - \omega^+) - 1) \\
&+ f_i^{\text{neq}-}(a_2(1 - \omega^-) - a_3(1 - \omega^-) - a_4 - a_5(1 - \omega^-) + 1 - K^- \omega^-) \\
&- \partial_t f_i^{\text{eq}+} + \partial_t f_i^{\text{eq}-} - \underline{\partial_t f_i^{\text{neq}+} + \partial_t f_i^{\text{neq}-}} - \frac{\partial_t^2}{2} f_i^{\text{eq}+} + \frac{\partial_t^2}{2} f_i^{\text{eq}-}. \tag{D2}
\end{aligned}$$

Steps 3 and 4: In these steps, the *diffusive scaling* is assumed. The explicit consequence is that we disregard the terms underlined in the Eq. (D2) of the previous step. However, this assumption is also implicitly considered using the Chapman-Enskog expansion of the nonequilibrium in the form of Eq. (28):

$$\begin{aligned}
[f_i^{\text{eq}+}(-a_4 - a_5) + f_i^{\text{eq}-}(a_4 + a_5 + 2a_2)]_{x_W}^{t+1} &= f_i^{\text{eq}+}(a_2 + a_3 - 1) + f_i^{\text{eq}-}(a_2 - a_3 + 1) \\
&+ (\partial_t f_i^{\text{eq}-} - \Lambda^- \partial_t^2 f_i^{\text{eq}+})[-a_2(\tau^+ - 1) - a_3(\tau^+ - 1) - \tau^+ a_4 - a_5(\tau^+ - 1) + \tau^+] \\
&+ \partial_t f_i^{\text{eq}+}[-a_2(\tau^+ - 1) - a_3(\tau^+ - 1) - \tau^+ a_4 - a_5(\tau^+ - 1) + \tau^+ - 1] \\
&+ (\partial_t f_i^{\text{eq}+} - \Lambda^+ \partial_t^2 f_i^{\text{eq}-})[-a_2(\tau^- - 1) + a_3(\tau^- - 1) + \tau^- a_4 + a_5(\tau^- - 1) - \tau^- + K^-] \\
&+ \partial_t f_i^{\text{eq}-}[-a_2(\tau^- - 1) + a_3(\tau^- - 1) + \tau^- a_4 + a_5(\tau^- - 1) - \tau^- + \tau^- K^- \omega^- + 1]. \tag{D3}
\end{aligned}$$

Step 5:

$$\alpha^+ = a_2 + a_3 - 1, \tag{D4a}$$

$$\alpha^- = a_2 - a_3 + 1, \tag{D4b}$$

$$\alpha_W^+ = -a_4 - a_5, \tag{D4c}$$

$$\alpha_W^- = a_4 + a_5 + 2a_2, \tag{D4d}$$

$$\beta^+ = -a_2(\tau^- - 1) + a_3(\tau^- - 1) + \tau^- a_4 + a_5(\tau^- - 1) - \tau^- + K^-, \tag{D4e}$$

$$\beta^- = -a_2(\tau^+ - 1) - a_3(\tau^+ - 1) - \tau^+ a_4 - a_5(\tau^+ - 1) + \tau^+, \tag{D4f}$$

$$\tau^+ = \beta^- - 1, \tag{D4g}$$

$$\tau^- = \beta^+ + 1, \tag{D4h}$$

$$\gamma^+ = -\Lambda^- \beta^-, \tag{D4i}$$

$$\gamma^- = -\Lambda^+ \beta^+. \tag{D4j}$$

Step 6: Taylor expanding the symmetric and antisymmetric components of the RHS of Eq. (30) leads to

$$\alpha_W^+ f_i^{\text{eq}+}\Big|_{x_W}^{t+1} \approx \alpha_W^+ \left(1 + \partial_t + q c_{i,\alpha} \partial_\alpha + \frac{\partial_t^2}{2} + \underline{q c_{i,\alpha} \partial_t \partial_\alpha} + \frac{q^2}{2} (c_{i,\alpha} \partial_\alpha)^2 \right) f_i^{\text{eq}+}\Big|_{x_F}^t, \tag{D5}$$

$$\alpha_w^- f_i^{\text{eq}-} \Big|_{x_w}^{t+1} \approx \alpha_w^- \left(1 + \partial_t + q c_{i,\alpha} \partial_\alpha + \cancel{\partial_t^2/2} + \cancel{q c_{i,\alpha} \partial_t \partial_\alpha} + \frac{q^2}{2} (c_{i,\alpha} \partial_\alpha)^2 \right) f_i^{\text{eq}-} \Big|_{x_f}^t, \quad (\text{D6})$$

where the striped terms are neglected under the *diffusive scaling* assumption thanks to Eq. (C6). Then, noting that from the natural choice $\alpha^- = \alpha_w^-$ follows $\alpha^+ = \alpha_w^+$ and equating symmetric and antisymmetric components of Eq. (30) we get the sum of the following:

$$\begin{aligned} \alpha^+ \left(\cancel{\lambda} + \partial_t + q c_{i,\alpha} \partial_\alpha + \cancel{\frac{\partial_t^2}{2}} + \cancel{q c_{i,\alpha} \partial_t \partial_\alpha} + \frac{q^2}{2} (c_{i,\alpha} \partial_\alpha)^2 \right) f_i^{\text{eq}+} \\ \approx (\cancel{\alpha^+} + \tau^+ \partial_t + \beta^+ c_{i,\alpha} \partial_\alpha + \cancel{\nu^+ \partial_t^2} + \cancel{\theta^+ c_{i,\alpha} \partial_t \partial_\alpha} + \gamma^+ (c_{i,\alpha} \partial_\alpha)^2) f_i^{\text{eq}+}, \end{aligned} \quad (\text{D7a})$$

$$\begin{aligned} \alpha^- \left(\cancel{\lambda} + \partial_t + \cancel{q c_{i,\alpha} \partial_\alpha} + \cancel{\frac{\partial_t^2}{2}} + \cancel{q c_{i,\alpha} \partial_t \partial_\alpha} + \frac{q^2}{2} (c_{i,\alpha} \partial_\alpha)^2 \right) f_i^{\text{eq}-} \\ \approx (\cancel{\alpha^-} + \tau^- \partial_t + \cancel{q \alpha^- c_{i,\alpha} \partial_\alpha} + \cancel{\nu^- \partial_t^2} + \cancel{\theta^- c_{i,\alpha} \partial_t \partial_\alpha} + \gamma^- (c_{i,\alpha} \partial_\alpha)^2) f_i^{\text{eq}-}, \end{aligned} \quad (\text{D7b})$$

where the terms barred with “/” are either simplified or a consequence of setting $\beta^- = q\alpha^-$, while the canceled by “\” ones are neglected under the assumption of *diffusive scaling* thanks to Eq. (C6). Equation (D7b) is reduced at steady state when $\gamma^- = q^2/2$. This last result is achieved with the parabolic MR schemes. In our current proposition we choose $K^- = K_1^-$ such that $\gamma^- = \alpha^- \Lambda$ following the parametrization of MGLI schemes [20] (see also Appendix D3). Thus, $K^- = K_1^-$ formally preserves the parabolic accuracy at steady state when $\Lambda = q^2/2$. In other terms, using K_1^- , the considered scheme reduces to the parabolic HW when $\Lambda = 1/8$ and $q = 1/2$ in the absence of the external forcing. The choice $\Lambda = 1/8$ is most general and isotropic, it extends for forcing with the modified boundary equilibrium value following [13]. Otherwise, $\Lambda = 3/16$ replaces $\Lambda = 1/8$ for Poiseuille Stokes flow with standard HW rule.

As opposed to ELI, LI/MGLI schemes enforce in the closure relation $\alpha^+ = 0$ with an appropriate selection of the interpolation coefficients a_i , and then they vanish the leading-order equilibrium term $\alpha^+ f_i^{\text{eq}+}$ [20]. Consequently, they do not need to approximate and prescribe $f_i^{\text{eq}+}$ on the wall (i.e., the two LHS of Eqs. (D7) are null). More advanced MR parabolic schemes also enforce $\beta^+ = 0$ and $\gamma^+ = 0$ to avoid dependence from linear and parabolic pressure terms [13], respectively, $\beta^+ c_{i,\alpha} \partial_\alpha f_i^{\text{eq}+}$ and $\gamma^+ (c_{i,\alpha} \partial_\alpha)^2 f_i^{\text{eq}+}$. In contrast, ELI keeps α^+ free and we will examine in future work whether if possible to enforce $\beta^+ - q\alpha^+ = 0$ and $\gamma^+ - q^2/2\alpha^+ = 0$.

As the last note of time-dependent closure, we remind that the time terms in Eq. (D7) appear herein in the specific form that follows the assumption that the wall populations are set at integer time steps t . This is not a unique possibility. But an extensive time-dependent analysis is out of the scope of the present article, and it is left to future investigations.

2. Coefficients of the closure relation

In the following lines, we report the final expression of the coefficients appearing in Eq. (29):

$$\alpha^+ = a_2 + a_3 - 1, \quad \alpha^- = 1 + a_2 - a_3, \quad (\text{D8a})$$

$$\tau^+ = \beta^- - 1, \quad \tau^- = \beta^+ + 1, \quad (\text{D8b})$$

$$\beta^+ = -\frac{\gamma^-}{\Lambda^+}, \quad \beta^- = \alpha^- q, \quad (\text{D8c})$$

$$\gamma^+ = -\beta^- \Lambda^-, \quad \gamma^- \in \{\gamma_N^-, \gamma_S^-, \gamma_C^-\}, \quad (\text{D8d})$$

$$\gamma_N^- = 2(1 - a_3)\Lambda + \Lambda^+[1 - q(1 + a_2) + a_3(1 + q) - K^-], \quad (\text{D9a})$$

$$\gamma_S^- = 2a_2\Lambda - \Lambda^+[a_2 - q(1 - a_3) - a_2q + K^-], \quad (\text{D9b})$$

$$\gamma_C^- = \alpha^- \Lambda + \frac{1}{2}\Lambda^+(1 + a_3 - a_2 - 2K^-). \quad (\text{D9c})$$

3. Computation of K^-

After imposing the condition $\beta^- = q\alpha^-$, the steady-state closure relation depends on the viscous (symmetric) relaxation time Λ^+ at steady state through only the coefficient γ^- . Thus, we can define the set

$$\mathcal{K}^- = \left\{ K^- \in \mathbb{R} \mid \frac{\partial \gamma^-}{\partial \Lambda^+} = 0 \right\} \quad (\text{D10})$$

that contains all the possible values of K^- that make the closure relations and, as a consequence, the boundary condition *viscosity independent*, i.e., independent from the symmetric relaxation time $\tau^+ = \Lambda^+ + 1/2$. In particular, we consider two possible K^-

elements of \mathcal{K}^- for each combination of a_2 and a_3 :

$$\begin{aligned} K_1^- : \gamma^- &= \Lambda \alpha^-, \\ K_2^- : \gamma^- &= \gamma_X^- - \int \frac{\partial \gamma_X^-}{\partial \Lambda^+} d\Lambda^+, \quad X \in \{N, S, C\}, \end{aligned} \quad (\text{D11})$$

where K_1^- represents the same parametrization used for the LI/MGLI schemes [20], while the K_2^- follows from asking that γ^- depends upon Λ^\pm only through Λ and has the advantage of being collision model independent. The idea followed by the first type of parametrization is to choose K_1^- such that when $q = 1/2$ the second order error associated to $(c_{\bar{i},\alpha} \partial_\alpha)^2 f_i^{\text{eq}}$ is canceled when $\Lambda = 1/8$. Regarding K_2^- , using Eq. (D9a), we get

$$K_2^- = \begin{cases} 1 - q(1 + a_2) + a_3(1 + q), & \text{if } \gamma^- = \gamma_N^- \text{ (NELI)}, \\ 2(1 - a_3) - a_2(1 - q), & \text{if } \gamma^- = \gamma_S^- \text{ (SELI)}, \\ 1/2(1 + a_3 - a_2), & \text{if } \gamma^- = \gamma_C^- \text{ (CELI)}. \end{cases} \quad (\text{D12})$$

APPENDIX E: TECHNICAL DETAILS OF JEFFERY'S ORBIT TEST CASE

1. Force computation

There exist two main ways to compute the force and torque acting on the surfaces: the stress tensor integration [87] and the momentum exchange algorithm [7]. As recommended by Mei *et al.* [88], the momentum exchange algorithm is used for the computation of the force in the following section.

There are different numerical approaches to compute the momentum exchange from the fluid to the surface [6,88–93] that have been summarized by Tao *et al.* in Ref. [80]. For the experiments in this paper we have decided to adopt the method described in Ref. [93]. In Ref. [93] Wen *et al.* propose the following receipt to compute the force exerted by one node on the boundary

$$\mathbf{F} = \left\{ \sum_i -((\mathbf{c}_i - \mathbf{u}_w) f_i(\mathbf{x}_F) - (\mathbf{c}_i - \mathbf{u}_w) f_i^*(\mathbf{x}_F)) \right\}_{\text{out}}, \quad (\text{E1})$$

where \mathbf{F} is the force acting on the boundary surface due to one fluid lattice and the index “out” means that when the boundary is described as a closed surface, the force computation has to be carried out only for the “external” fluid.

2. Qualitative approach to evaluate torque oscillations

The theoretical value of the torque acting on the ellipsoid (or ellipsoidal cylinder) changes over time. If the ellipsoid inertia is small, then the magnitude of the torque oscillation exceeds the value of the theoretical torque. Unfortunately, the analytical value of the torque is not available and this makes it impossible to compute the oscillation because the baseline solution is unknown. To give a qualitative representation of the evolution of the torque-squared fluctuation, we decided to compute a smooth numerical baseline solution using interpolating polynomials. This baseline regular numerical solution is then used to compute the squared fluctuation of the torque (TSF) over time. The TSF of the torque computed in this way is noisy and not precise enough to obtain quantitative results. Nevertheless, we can use it to perform a second interpolation with a polynomial of the same order to get a qualitative estimation of the TSF evolution over time and use it to compare visually different methods.

In detail, the first polynomial least-squares interpolation is of order $n = 30$ and reads

$$T_{\text{ip},n}(t_j) = \operatorname{argmin} \left(\sum_{j=0}^k |p_n(t_j) - T_j(t_j)|^2 \right), \quad (\text{E2})$$

where p_n is a polynomial of order n , T_j is the torque at time step t_j , and $T_{\text{ip},n}$ is the best fitting polynomial of order n . After the computation of the torque-squared fluctuation (TSF),

$$\text{TSF} = (T - T_{\text{ip},n})^2, \quad (\text{E3})$$

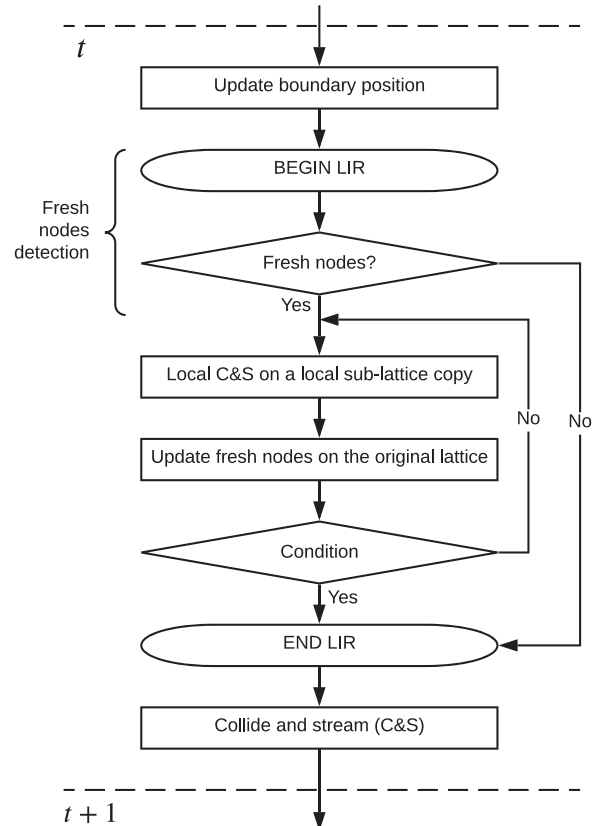


FIG. 18. The modified LIR algorithm.

a second interpolating polynomial of the same order is computed for the fluctuations,

$$\text{TSF}_{\text{ip},n}(t_j) = \operatorname{argmin} \left(\sum_{j=0}^k |p_n(t_j) - T_{\text{ip},n,j}(t_j)|^2 \right). \quad (\text{E4})$$

This procedure allows to produce regular and qualitative graphs of the torque-squared fluctuations in time.

3. Local iteration refilling

The local iteration refilling (LIR) proposed in Ref. [45] is reinterpreted making sure that the LIR is applied *before* the global collide and stream, right after the boundary movement. This detail guarantees that the streaming step does not move wrong populations outside the *fresh nodes* before the application of the LIR. The modified algorithm is represented in Fig. 18. From our test, we observed that we get the best results for few iterations (1...3), without the need of more complex stop conditions.

-
- [1] Y. Thorimbert, F. Marson, A. Parmigiani, B. Chopard, and J. Latt, *Comput. Fluids* **166**, 286 (2018).
- [2] C. Huber, A. Parmigiani, J. Latt, and J. Dufek, *Water Resour. Res.* **49**, 6371 (2013).
- [3] G. Silva, L. Talon, and I. Ginzburg, *J. Comput. Phys.* **335**, 50 (2017).
- [4] C. Kotsalos, J. Latt, and B. Chopard, *J. Comput. Phys.* **398**, 108905 (2019).
- [5] S. Leclaire, A. Parmigiani, O. Malaspinas, B. Chopard, and J. Latt, *Phys. Rev. E* **95**, 033306 (2017).
- [6] I. Ginzburg and P. M. Adler, *J. Physique II* **4**, 191 (1994).
- [7] A. J. C. Ladd, *J. Fluid Mech.* **271**, 285 (1994).
- [8] I. Ginzburg and D. d'Humières, *Phys. Rev. E* **68**, 066614 (2003).
- [9] T. Krüger, H. Kusumaatmaja, A. Kuzmin, O. Shardt, G. Silva, and E. M. Viggen, *The Lattice Boltzmann Method: Principles and Practice*, Graduate Texts in Physics (Springer International Publishing, Berlin, 2017).
- [10] I. Ginzbourg and D. d'Humières, *J. Stat. Phys.* **84**, 927 (1996).
- [11] S. Khirevich, I. Ginzburg, and U. Tallarek, *J. Comput. Phys.* **281**, 708 (2015).
- [12] I. Ginzburg, *J. Comput. Phys.* **431**, 109986 (2021).
- [13] I. Ginzburg, *J. Comput. Sci.*, 101215 (2020).
- [14] M. Junk and Z. Yang, *Phys. Rev. E* **72**, 066701 (2005).
- [15] B. Chun and A. J. C. Ladd, *Phys. Rev. E* **75**, 066705 (2007).
- [16] W. Zhao and W.-A. Yong, *J. Comput. Phys.* **329**, 1 (2017).
- [17] S. Tao, Q. He, B. Chen, X. Yang, and S. Huang, *Comput. Math. Appl.* **76**, 1593 (2018).
- [18] S. Liu, T. Zhou, S. Tao, Z. Wu, and G. Yang, *Int. J. Mod. Phys. C* **30**, 1950041 (2019).
- [19] G. Silva and I. Ginzburg, *Philos. Trans. R. Soc. London A* **378**, 20190404 (2020).
- [20] I. Ginzburg and F. Verhaeghe, *Commun. Comput. Phys.* **3**, 427 (2008).
- [21] I. Ginzburg and F. Verhaeghe, *Commun. Comput. Phys.* **3**, 519 (2008).
- [22] C. Peng, O. M. Ayala, and L.-P. Wang, *Comput. Fluids* **192**, 104233 (2019).
- [23] P. Zhang, S. A. Galindo-Torres, H. Tang, G. Jin, and L. Li, *arXiv:1903.01111*.
- [24] A. De Rosis, S. Ubertini, and F. Ubertini, *J. Sci. Comput.* **61**, 477 (2014).
- [25] M. Bouzidi, M. Firdaouss, and P. Lallemand, *Phys. Fluids* **13**, 3452 (2001).
- [26] R. M. Dazhi Yu and W. Shyy, in *Proceedings of the 41st Aerospace Sciences Meeting and Exhibit* (American Institute of Aeronautics and Astronautics, Reston, VA, 2003).
- [27] G. Silva and V. Semiao, *Phys. Rev. E* **96**, 013311 (2017).
- [28] G. Silva, *Phys. Rev. E* **98**, 023302 (2018).
- [29] C. Rettinger and U. Rude, *Comput. Fluids*, **154**, 74 (2017).
- [30] W. Zhao, J. Huang, and W.-A. Yong, *Multiscale Model. Simul.* **17**, 854 (2019).
- [31] L. Wang, S. Tao, X. Meng, K. Zhang, and G. Lu, *Phys. Rev. E* **101**, 063307 (2020).
- [32] X. Meng, L. Wang, W. Zhao, and X. Yang, *Adv. Water Resour.* **141**, 103583 (2020).
- [33] C. Peng, O. M. Ayala, J. C. Brändle de Motta, and L.-P. Wang, *Comput. Fluids* **192**, 104251 (2019).
- [34] Q. Zou and X. He, *Phys. Fluids* **9**, 1591 (1997).
- [35] O. Filippova and D. Hänel, *Comput. Fluids* **26**, 697 (1997).
- [36] O. Filippova and D. Hänel, *J. Comput. Phys.* **147**, 219 (1998).
- [37] S. Succi, *The Lattice Boltzmann Equation: For Complex States of Flowing Matter*, 1st ed. (Oxford University Press, Oxford, UK, 2018).
- [38] Z. Guo and C. Shu, *Lattice Boltzmann Method and Its Applications in Engineering*, Advances in Computational Fluid Dynamics (World Scientific, Singapore, 2013).
- [39] R. Mei, L.-S. Luo, and W. Shyy, *J. Comput. Phys.* **155**, 307 (1999).
- [40] Z. Yang, Analysis of Lattice Boltzmann Boundary Conditions, Ph.D. thesis, University of Konstanz, 2007.
- [41] R. W. Nash, H. B. Carver, M. O. Bernabeu, J. Hetherington, D. Groen, T. Krüger, and P. V. Coveney, *Phys. Rev. E* **89**, 023303 (2014).
- [42] D. R. Noble and J. R. Torczynski, *Int. J. Mod. Phys. C* **09**, 1189 (1998).
- [43] R. Cornubert, D. d'Humières, and D. Levermore, *Physica D* **47**, 241 (1991).
- [44] P. A. Skordos, *Phys. Rev. E* **48**, 4823 (1993).
- [45] L. Chen, Y. Yu, J. Lu, and G. Hou, *Int. J. Numer. Methods Fluids* **74**, 439 (2014).
- [46] J. Latt, O. Malaspinas, D. Kontaxakis, A. Parmigiani, D. Lagrava, F. Brogi, M. B. Belgacem, Y. Thorimbert, S. Leclaire, S. Li, F. Marson, J. Lemus, C. Kotsalos, R. Conradin, C. Coreixas, R. Petkantchin, F. Raynaud, J. Beny, and B. Chopard, *Comput. Math. Appl.*, **81**, 334 (2021).
- [47] L. Boltzmann, *Lectures on Gas Theory* (Dover Publications, New York, 1995).
- [48] D. Hilbert, Grundzüge einer allgemeinen Theorie der linearen Integralgleichungen (B. G. Teubner, Leipzig und Berlin, 1912).
- [49] S. Chapman, T. Cowling, D. Burnett, and C. Cercignani, *The Mathematical Theory of Non-uniform Gases: An Account of the Kinetic Theory of Viscosity, Thermal Conduction and Diffusion*

- in Gases*, Cambridge Mathematical Library (Cambridge University Press, Cambridge, UK, 1953).
- [50] Carlo Cercignani, *The Boltzmann Equation and Its Applications*, edited by F. John, J. E. Marsden, and L. Sirovich, Applied Mathematical Sciences, Vol. 67 (Springer, New York, NY, 1988).
- [51] C. Cercignani, R. Illner, and M. Pulvirenti, *The Mathematical Theory of Dilute Gases* edited by F. John, J. E. Marsden, and L. Sirovich (Springer, New York, 1994).
- [52] C. Cercignani and E. Gabetta, eds., *Transport Phenomena and Kinetic Theory: Applications to Gases, Semiconductors, Photons, and Biological Systems*, Modeling and Simulation in Science, Engineering and Technology (Birkhauser, Boston, 2007).
- [53] G. M. Kremer, *An Introduction to the Boltzmann Equation and Transport Processes in Gases*, Interaction of Mechanics and Mathematics (Springer, Berlin/New York, 2010).
- [54] P. L. Bhatnagar, E. P. Gross, and M. Krook, *Phys. Rev.* **94**, 511 (1954).
- [55] P. Welander, *Arkiv Fysik* **7**, 507 (1954).
- [56] Y. H. Qian, D. d’Humières, and P. Lallemand, *Europhys. Lett.* **17**, 479 (1992).
- [57] X. Shan and X. He, *Phys. Rev. Lett.* **80**, 65 (1998).
- [58] X. Shan, X.-F. Yuan, and H. Chen, *J. Fluid Mech.* **550**, 413 (2006).
- [59] P. J. Dellar, *Comput. Math. Appl.* **65**, 129 (2013).
- [60] G. R. McNamara and G. Zanetti, *Phys. Rev. Lett.* **61**, 2332 (1988).
- [61] F. J. Higuera and J. Jiménez, *Europhys. Lett.* **9**, 663 (1989).
- [62] C. Coreixas, G. Wissocq, B. Chopard, and J. Latt, *Philos. Trans. R. Soc. London A* **378**, 20190397 (2020).
- [63] C. Coreixas, B. Chopard, and J. Latt, *Phys. Rev. E* **100**, 033305 (2019).
- [64] D. d’Humières, in *Rarefied Gas Dynamics: Theory and Simulations*, Progress in Astronautics and Aeronautics (American Institute of Aeronautics and Astronautics, Reston, VA, 1994), pp. 450–458.
- [65] P. Lallemand and L.-S. Luo, *Phys. Rev. E* **61**, 6546 (2000).
- [66] D. d’Humières, I. Ginzburg, M. Krafczyk, P. Lallemand, and L.-S. Luo, *Philos. Trans. R. Soc. London A* **360**, 437 (2002).
- [67] I. Ginzburg, *Adv. Water Resour.* **28**, 1171 (2005).
- [68] I. Ginzburg, *J. Stat. Phys.* **126**, 157 (2007).
- [69] P. J. Dellar, *J. Comput. Phys.* **190**, 351 (2003).
- [70] D. d’Humières and I. Ginzburg, *Comput. Math. Appl.* **58**, 823 (2009).
- [71] I. Ginzburg, D. d’Humières, and A. Kuzmin, *J. Stat. Phys.* **139**, 1090 (2010).
- [72] J. L. de Lagrange, *Leçons élémentaires sur les Mathématiques, données à l’École normale, en 1795* (Gauthier-Villars, 1812), Vol. 7.
- [73] J. Sylvester, *London, Edinburgh Dublin Philos. Mag. J. Sci.* **16**, 267 (1883).
- [74] S. Gsell, U. D’Ortona, and J. Favier, *J. Comput. Phys.* **429**, 109943 (2020).
- [75] M. Wittmann, T. Zeiser, G. Hager, and G. Wellein, *Comput. Math. Appl. Mesoscopic Methods Eng. Sci.* **65**, 924 (2013).
- [76] J. Latt, C. Coreixas, and J. Beny, *PLOS ONE* **16**, e0250306 (2020).
- [77] X. Yin, G. Le, and J. Zhang, *Phys. Rev. E* **86**, 026701 (2012).
- [78] B. Ahrenholz, J. Tölke, and M. Krafczyk, *Int. J. Comput. Fluid Dynam.* **20**, 369 (2006).
- [79] M. Emin Erdoğan, *Int. J. Non Linear Mech.* **37**, 1091 (2002).
- [80] S. Tao, J. Hu, and Z. Guo, *Comput. Fluids* **133**, 1 (2016).
- [81] G. B. Jeffery and L. N. G. Filon, *Proc. R. Soc. London A* **102**, 161 (1922).
- [82] M. Haussmann, N. Hafen, F. Raichle, R. Trunk, H. Nirschl, and M. J. Krause, *Comput. Math. Appl.* **80**, 671 (2020).
- [83] A. Caiazzo and M. Junk, *Comput. Math. Appl.* **55**, 1415 (2008).
- [84] X. Li, F. Jiang, and C. Hu, *Comput. Fluids* **129**, 33 (2016).
- [85] I. Ginzburg and G. Silva, *Phys. Fluids* **33**, 057104 (2021).
- [86] A. Gorban and I. Karlin, *Bull. Amer. Math. Soc.* **51**, 187 (2014).
- [87] T. Inamuro, K. Maeba, and F. Ogino, *Int. J. Multiphase Flow* **26**, 1981 (2000).
- [88] R. Mei, D. Yu, W. Shyy, and L.-S. Luo, *Phys. Rev. E* **65**, 041203 (2002).
- [89] Y. Hu, D. Li, S. Shu, and X. Niu, *Phys. Rev. E* **91**, 033301 (2015).
- [90] E.-J. Ding and C. K. Aidun, *J. Stat. Phys.* **112**, 685 (2003).
- [91] Y. Chen, Q. Cai, Z. Xia, M. Wang, and S. Chen, *Phys. Rev. E* **88**, 013303 (2013).
- [92] H. Li, X. Lu, H. Fang, and Y. Qian, *Phys. Rev. E* **70**, 026701 (2004).
- [93] B. Wen, C. Zhang, Y. Tu, C. Wang, and H. Fang, *J. Comput. Phys.* **266**, 161 (2014).